ACS NANO

www.acsnano.org

ARTICLE

Core–Shell Magnetic Micropillars for Reprogrammable Actuation

Ke Ni,[#] Qi Peng,[#] Enlai Gao,[#] Kun Wang, Qian Shao, Houbing Huang, Longjian Xue, and Zhengzhi Wang*

Cite This: *ACS Nano* 2021, 15, 4747–4758

Read Online

ACCESS | Metrics & More | Article Recommendations | Supporting Information

ABSTRACT: **Stimuli-responsive micro/nanostructures that exhibit not only programmable but also reprogrammable actuation behaviors are highly desirable for various advanced engineering applications (*e.g.*, anticounterfeiting, information encoding, dynamic imaging and display, microrobotics, *etc.*) but yet to be realized with state-of-the-art technologies. Here we report a concept and a corresponding experimental technique for core–shell magnetic micropillars enabling simultaneously programmable and reprogrammable actuations using a simple magnetic field. The micropillars are composed of elastomeric hollow shells for shaping encapsulated with liquid magnetic nanocomposite resin cores for actuating. The spatial distribution of the magnetic nanoparticles inside the resin channels can be dynamically modulated within individual micropillars, which consequently regulates the magnetomechanical responses of the pillars upon actuation (bending deformation varied near 1 order of magnitude under the same actuation field). We demonstrate that the micropillars with contrasting bending responses can be configured in an arbitrary spatial pattern by direct magnetic writing, and the written pattern can then be easily magnetically erased to facilitate next-round rewriting and reconfiguration. This reprogrammable actuation capability of the micropillars is further demonstrated by their potential applications for rewritable paper and recyclable displays, where various microscale characteristics can be controlled to dynamically appear and disappear at the same or different locations of one single micropillar array. The core–shell magnetic micropillars reported here provide a universal prototype for reprogrammable responsive micro/nanostructures through rational design and facile fabrication from conventional materials.**

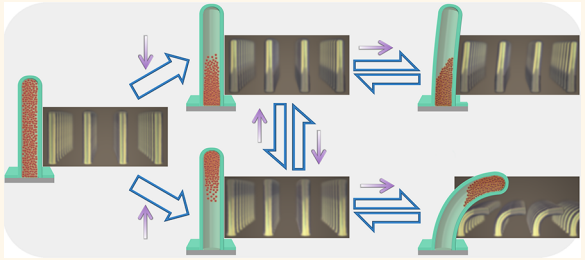

KEYWORDS: *stimuli-responsive microstructures, magnetic micropillars, core–shell structures, reprogrammable actuation, bending*

Stimuli-responsive micro/nanostructures that are able to execute programmed and on-demand mechanical deformations upon external actuations (optical, electromagnetic, thermal, chemical, *etc.*) have been increasingly studied lately[1−6] due to their potential applications in various fields including soft robotics,[7−12] tunable metasurfaces,[13−19] high-precision sensors and actuators,[20−23] and biological devices,[24−27] among many others.[28−33] For the responsive micro/nanostructures, it is highly desirable to achieve both programmable (*i.e.*, the structures can deform in a predesigned manner) and reprogrammable (*i.e.*, the structures can reversibly and recurrently deform into multiple configurations as demanded) actuated deformations such that various shapes/patterns and functionalities can be realized using one single material and structure system.[34−36] Although significant advances have been made in designing and fabricating the programmable responsive micro/nanostructures so far,[3,5,7,8,10−14,16−21,25−33] the actuated configurations of current structures are usually fixed once the fabrication is completed, showing no further shape/pattern reconfiguration capability.[3,10,12,14,16−21,25−31] There have been a few efforts to achieve reprogrammable actuations either by using specific stimuli-responsive materials (*e.g.*, liquid crystal elastomers/networks and shape-memory polymers)[37−41] or by adopting complex geometrical/structural designs combined with multiple actuation steps.[7,8,11,29,32,36,42−45] However, structures in such efforts are limited to a relatively large scale (usually millimeters and above), and the reprogrammable actuations are difficult to extend to more general material systems.[7,8,11,29,32,37−45] Therefore, it still remains a great challenge to achieve dynamic and multifunctional shape/pattern manipulations in one micro/nanostructure system, and a universal strategy for

Received: November 6, 2020
Accepted: February 18, 2021
Published: February 22, 2021

https://dx.doi.org/10.1021/acsnano.0c09298
ACS Nano 2021, 15, 4747–4758

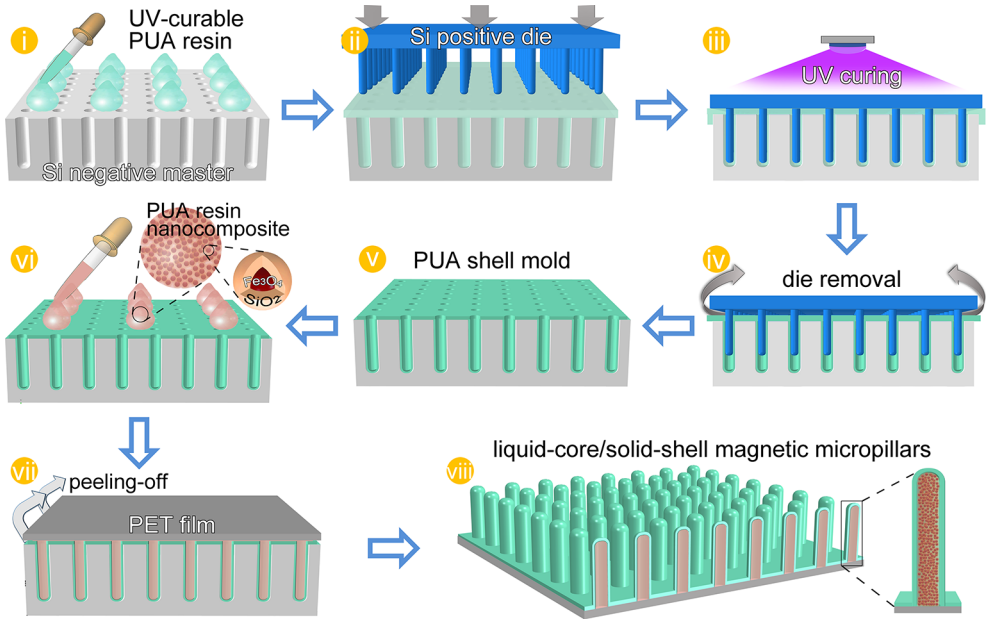

Figure 1. Schematic diagram of the processing steps for the fabrication of the core–shell magnetic micropillars: (1) filling cavities of silicon negative master with UV-curable PUA resin; (2) aligning and pressing predesigned silicon positive die (stiff micropillar array) into the filled cavities to squeeze out and hollow the infiltrated resin; (3) *in situ* UV curing and solidifying the hollowed PUA resin; (4) mechanically removing the positive die and leaving (5) hollow PUA shell mold supported in the negative master; (6) filling the cavities of the shell mold with uncurable, homogeneous PUA/Fe_3O_4@SiO_2 nanocomposite resin; (7) covering and sealing the infiltrated composite resin with PET film and peeling them (PET film, infiltrated resin, and PUA shell mold) off from the negative master and obtaining (8) core–shell magnetic micropillars composed of a solid PUA shell encapsulating a liquid magnetic nanocomposite resin.

reprogrammable actuations is yet to be realized with existing material systems and state-of-the-art technologies.

Among the different actuation strategies to trigger the mechanical deformations of the responsive structures, the use of a magnetic field has been one of the most common due to its rapid response, remote and untethered control, and low cost.[3,5−8,10−12,14,16−19,25,27,28,30,36−38,42,43,46−50] For the fabrication of a magnetic-responsive micro/nanostructure, the magnetic media for actuating (usually dispersed magnetic nanoparticles or nanowires) are often premixed in a flexible polymer solvent matrix (most often elastomers) and then cured and solidified together once the desired shapes/patterns of the nanocomposites are formed.[10−12,14,16−18,25,30,32,43,46−50] In this way, the spatial distribution and magnetization profile of the magnetic media inside the cured matrix are determined permanently, and thus the obtained structures can present only one single actuation mode upon applying a specific external magnetic field.[14,16−18,25,30,46−48] Although the deformations of the responsive structures can be adjusted by varying the actuation conditions such as the intensity and direction of the actuation field, such adjustments are only limited to the extent and direction of the deformations, and an advanced control over the actuated and reactuated shapes and/or patterns of the whole structure remains thus far inaccessible.[14,16−18,25,30,46−48] Considering that the magnetic media can be easily and dynamically modulated when dispersed in a liquid environment,[51−54] and the actuation of the responsive micro/nanostructures would be more controllable and configurable if the magnetic mixture is in a liquid state, instead of a cured solid state, this model is adopted for actuating the deformations of the structures.

To demonstrate this concept of "actuating in liquid" and achieve reprogrammable and reconfigurable actuations, herein we develop a different type of magnetic-responsive micropillars composed of solid elastomer hollow shells for shaping encapsulated with liquid magnetic nanocomposite resin cores for actuating. The spatial distribution and magnetization profile of the magnetic nanoparticles inside the resin channels can be dynamically modulated to tune the bending responses of the core–shell micropillars upon actuation. By concentrating the nanoparticles from the tip to the base region inside the pillars, the actuated bending deformation varies near 1 order of magnitude under the same actuation field. These micropillars with tunable magnetic responsivity can be patterned into a single array at any desired combinations to achieve heterogeneous, site-specific, and programmable actuations. The patterning of the combination can then be easily erased and reprogrammed by globally and locally applying a magnetic field to selectively redistribute the magnetic nanoparticles inside the resin channels of the micropillars, respectively. The core–shell magnetic micropillar arrays with both programmable and reprogrammable actuation capabilities are demonstrated to be promising for microscale rewritable paper and recyclable display applications. The concept and manufacturing technique for the liquid-core/solid-shell magnetic microstructures reported here are generic and may be extended to many other stimuli-responsive systems to achieve not only programmable and on-demand but also reconfigurable and reprogrammable mechanical responses.

RESULTS AND DISCUSSION

Fabrication and Characterizations of the Core–Shell Magnetic Micropillars. The core–shell magnetic micropillars were fabricated through a two-step template casting technique as shown schematically in Figure 1 and detailed in the Experimental Section. Briefly, a silicon negative master with patterned microcavities (diameter of 10 μm, depth of 80

https://dx.doi.org/10.1021/acsnano.0c09298
ACS Nano 2021, 15, 4747−4758

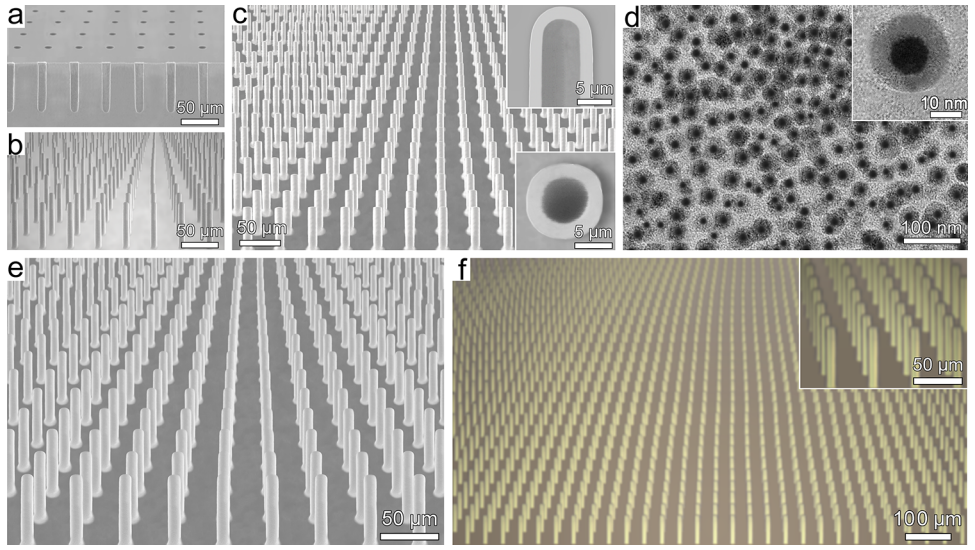

Figure 2. Morphology characterizations of the processing materials/structures and the fabricated core−shell magnetic micropillars. (a) Scanning electron microscope (SEM) image of the silicon negative master from the cross-sectional view, showing the patterned microcavities; (b) SEM image of the silicon positive die, showing the aligned micropillar array; (c) SEM images of the as-prepared hollow PUA shell mold (step 5 in Figure 1), showing the aligned and upright shell array. Insets showing SEM images of the longitudinal section (top) and the cross section (bottom) of a single micropillar shell. (d) Transmission electron microscope (TEM) images of the PUA/Fe_3O_4@SiO_2 nanocomposite resin, showing the homogeneous distribution of the nanoparticles inside the resin matrix and the core−shell structure of individual Fe_3O_4@SiO_2 nanoparticles (inset). (e) SEM and (f) large-area optical microscope images of the fabricated core−shell magnetic micropillars supported on a PET backing layer (step 8 in Figure 1), showing the well-aligned and structurally stable micropillar array.

μm, and center-to-center distance of 40 μm) was first filled with UV-curable polyurethane acrylate (PUA) resin (Figure 1, step 1). The PUA resin was adopted here because of its easy processability and tunable physical and mechanical properties.[55] A silicon micropillar array (diameter of 6 μm, height of 80 μm, and center-to-center distance of also 40 μm) was then used as a positive die to reshape and hollow the infiltrated resin. This was accomplished by carefully aligning and centering the micropillars with the cavities of the master and then pressing the aligned pillars into the infiltrated resin channels until there was a thin gap (~2 μm in thickness) left between the die and the master (Figure 1, step 2). The infiltrated resin was thus squeezed out and the remaining hollowed resin was cured and solidified by applying a sufficient UV irradiation (Figure 1, step 3). By mechanically removing the silicon die from the cured resin (Figure 1, step 4), a hollow PUA shell mold with patterned microcavities supported in the negative master was obtained (Figure 1, step 5). Subsequently, the shell mold was filled with uncurable, homogeneous PUA-based nanocomposite resin (Figure 1, step 6). The composites comprised pure PUA resin (without adding photoinitiators, viscosity of ~0.16 Pa.s) filled with 15 vol % superparamagnetic iron oxide nanoparticles coated with functionalized silica shells (Fe_3O_4@SiO_2, average diameter of ~30 nm). The infiltrated nanocomposite resin was then covered and sealed by a stiff polyethylene terephthalate (PET) film to avoid any liquid outflow (Figure 1, step 7). After peeling off the PET backing film, the PUA shell and the sealed magnetic liquid together from the master, core−shell magnetic micropillars composed of solid PUA shells encapsulating liquid magnetic nanocomposite resin were obtained (Figure 1, step 8).

The morphologies of the processing materials/structures and the fabricated core−shell magnetic micropillars were characterized by various microscopies, as the results show in Figure 2. Scanning electron microscope (SEM) images of the silicon master (Figure 2a) and the silicon micropillar die (Figure 2b) at the same magnification verified that the cavities of the master and the micropillars of the die exhibited the same depth/height and center-to-center space but different diameters. The smaller diameter of the die compared with that of the master facilitated the interposition and the resin-squeezing processes (Figure 1, steps 2 and 3). The prepared hollow PUA shell structure (Figure 1, step 5) after peeling off from the master was visualized by SEM with the typical images shown in Figure 2c. As can be seen, the aligned shells exhibited an outer diameter of ~10 μm, an inner diameter of ~6 μm, and a wall thickness of ~2 μm at both the stem and tip regions, consistent with the geometries of the master and the die. Besides, the cavities of the shells were sealed at the tips (top inset in Figure 2c), validating that the micropillar die did not penetrate through the resin channels during the interposition and these half-open cavities were just required for the subsequent filling-in of the magnetic nanocomposite resin. Transmission electron microscope (TEM) images of the PUA/Fe_3O_4@SiO_2 nanocomposite resin shown in Figure 2d verified the homogeneous distribution of the nanoparticles inside the resin matrix and the core−shell structure of individual nanoparticles. The silica shells were provided to improve the dispersibility of pure magnetic nanoparticles in the resin fluid.[51,56] SEM and optical microscope images of the fabricated core−shell magnetic micropillars supported on the PET backing layer (Figure 1, step 8) given in Figure 2e and f showed the perfectly aligned and structurally stable micropillar array, validating the successful fabrication of the liquid-core/solid-shell microstructures using the proposed methods shown in Figure 1.

Dynamic Modulation and Reprogrammable Actuation of the Core−Shell Magnetic Micropillars. Since the magnetic nanoparticles were now dispersed in the viscous resin channels and encased inside the elastomer micropillars, the spatial distribution of these particles along the pillars could be

https://dx.doi.org/10.1021/acsnano.0c09298
ACS Nano 2021, 15, 4747−4758

easily modulated through a magnetophoresis process by applying a redistribution magnetic field ($\mathbf{H}_r$) along the axial direction.[14,52] The micropillars with different spatial distributions of the magnetic media inside would then generate different magnetomechanical responses (bending deformations) upon applying a specific actuation field ($\mathbf{H}_a$) from the horizontal direction, according to our previous studies.[14,46] As shown in Figure 3a for the schematic diagrams and experimental observations of the nanoparticle redistributions and micropillar actuations, by applying a downward $\mathbf{H}_r$ (from pillar tip to the base) of ~200 mT and gradient of ~40 mT/mm generated by two parallel magnets placed in repulsive configuration (Figure S1, Supporting Information), the pristine micropillars with uniform distributions of the nanoparticles (UP) were transformed into pillars with the nanoparticles distributed toward the base regions (state 1 to state 2). On the contrary, if the direction of the $\mathbf{H}_r$ was switched to upward (from pillar base to the tip), the nanoparticles were concentrated to the tip regions of the pillars (state 1 to state 3). These different redistributions of the nanoparticles were confirmed by the captured transmission optical microscope images of the pillars, where the particle-enriched regions were visually darker than the particle-depleted ones (see Movies S1 and S2 for the transformation dynamics).

Upon applying a horizontal actuation field $\mathbf{H}_a$ (maximum of ~350 mT and gradient of ~25 mT/mm) generated by a single magnet approaching (Figure S2, Supporting Information), the transformed micropillars bent toward the direction of the $\mathbf{H}_a$ under the effect of the actuation forces ($\mathbf{F}_a$) exerted on the inner nanoparticles (state 2 to state 4 and state 3 to state 5 in Figure 3a; see Movies S3 and S4 for the bending movies). Due to the magnetic force being proportional to the local concentration of the nanoparticles, $\mathbf{F}_a$ was thus concentrated to the base regions (fixed ends) for those micropillars with particle-replete bases while to the tip regions (free ends) for those with particle-replete tips. These different distributions of the $\mathbf{F}_a$ induced contrasting actuated bending deformations of the pillars under the same $\mathbf{H}_a$ as observed in Figure 3a (states 4 and 5) and analyzed in detail later. We therefore referred to the pillars with particle-replete bases and particle-replete tips as small-deformation pillars (SDP) and large-deformation pillars (LDP), respectively. These two transformed states (*i.e.*, SDP and LDP) were also interconvertible by directly applying the corresponding $\mathbf{H}_r$ as depicted in Figure 3a (between states 2 and 3; see Movies S5 and S6 for the transformation dynamics). The actuated bending deformations of both the SDPs and LDPs were completely reversible, as all the micropillars returned to their original vertical configurations as soon as the $\mathbf{H}_a$ was removed (state 4 to state 2 and state 5 to state 3, Movies S3 and S4).

To quantitatively study the dynamics of the transformations between the various micropillars (UP, SDP, and LDP), we theoretically modeled the magnetophoresis-induced nanoparticle redistributions inside the confined resin channels by simulating the Brownian motions of the magnetic nanoparticles under the effect of $\mathbf{H}_r$.[57] For a magnetic nanoparticle submerged in a viscous liquid and subjected to a gradient magnetic field, the magnetic force ($\mathbf{F}_m$) applied to the particle can be calculated as[58]

$$\mathbf{F}_m = \frac{(\chi_p - \chi_r)V_p(\mathbf{B}\cdot\nabla\mathbf{B})}{\mu_0} \quad (1)$$

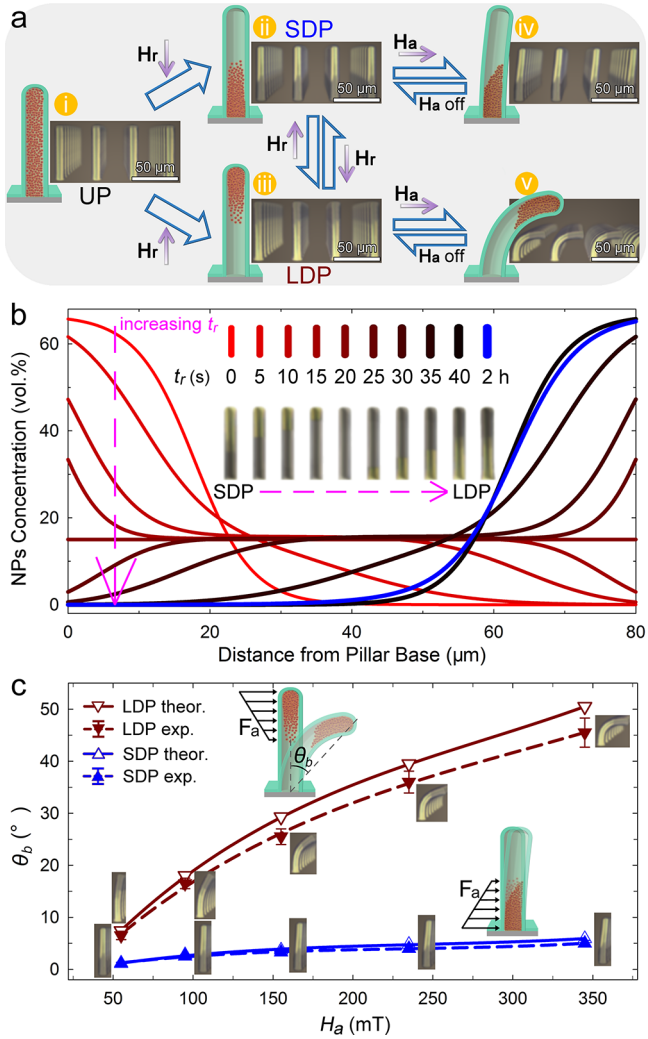

Figure 3. Modulation and actuation of the core−shell magnetic micropillars with contrasting nanoparticle distributions. (a) Schematic diagrams and experimental observations of the modulations and actuations: the uniform micropillars (UP, state 1) can be transformed into small deformation micropillars (SDP, state 2) or large deformation micropillars (LDP, state 3) by applying a downward or upward magnetic field H_r, respectively (Movies S1 and S2). The SDP and LDP are interconvertible by applying the corresponding H_r (Movies S5 and S6). The micropillars can then be actuated to contrasting bent configurations (states 4 and 5) by applying a horizontal actuation field H_a and returned to vertical configurations after removing H_a (Movies S3 and S4). Short arrows indicate the direction of the applied magnetic fields. (b) Theoretical predictions of the nanoparticle concentration along an individual micropillar at various times (t_r) after applying an upward H_r of 200 mT and 40 mT/mm. Blue line shows the result at 2 h after removing H_r. Insets show representative transmission optical microscope images of a micropillar during the transition from SDP to LDP. (c) Theoretically predicted (theor.) and experimentally observed (exp.) bending angle θ_b as a function of the actuation field H_a. The bigger insets show schematic diagrams of the simplified models for the actuated bending, while the smaller ones give the corresponding observed bent configurations. Error bars indicate the standard deviation of the experimental measurements.

where χ_p and χ_r are the magnetic susceptibility of the nanoparticle and the liquid resin, respectively, V_p is the volume of the particle, $\mathbf{B} = \mu_0\mathbf{H}$ is the magnetic flux density of the

https://dx.doi.org/10.1021/acsnano.0c09298
ACS Nano 2021, 15, 4747−4758

applied magnetic field where μ_0 is the permeability of the free space and $\mathbf{H}$ is the magnetic field at the center of the particle, and Vis the gradient operator. The magnetophoresis-driven migration of the nanoparticles inside the resin channels can be modeled as a diffusion transport process with the evolving spatiotemporal position of the particles described by the Langevin equation:[59]

$$m\frac{\mathrm{d}^2\mathbf{r}}{\mathrm{d}t^2} = \mathbf{F}_\mathrm{f}(t) + \mathbf{F}_\eta(t) + \mathbf{F}_\mathrm{m}(\mathbf{r}) \quad (2)$$

where m is the mass of the particle, $\mathbf{r}$ is the spatial position of the particle within the resin channel, and t is the time. The first term of the force $\mathbf{F}_\mathrm{f}(t)$ is the thermodynamic fluctuating force of the nanoparticles and the second term $\mathbf{F}_\eta(t)$ is the viscous dragging force (see details for the calculations in the Theories and Computations, Supporting Information). By adapting the experimental parameters adopted in the present study (Table S1, Supporting Information), we first calculated the magnetic field distribution and the magnetic force on a single nanoparticle upon applying the redistribution field $\mathbf{H}_\mathrm{r}$ (Figure S3, Supporting Information).[14] The evolving concentration profiles of the nanoparticles along the resin channels (*i.e.*, along the length direction of the micropillars) were then obtained by solving eq 2 using the finite difference method and accumulating the number of particles that reached each spatial position at various time steps.[60]

As shown in Figure S4, Supporting Information, for the calculated results of the transformation from UP to SDP, the concentration profile of the nanoparticles along the micropillar gradually transitioned from a constant of 15 vol % at time 0 (*i.e.*, before applying the downward $\mathbf{H}_\mathrm{r}$) to a continuous decrease from over 60 vol % at the pillar base to ~0 vol % spanning the middle to the pillar tip at 20 s after applying the $\mathbf{H}_\mathrm{r}$. These theoretical predictions of the evolution kinetics were in qualitative agreement with our experimental observations (Movie S1), where the nanoparticles gradually migrated from the pillar tip to the base and resulted in a gradual variation of the color scale of the pillar: from a uniform gray scale (UP) to a bottom-half-dark (particle-enriched) and top-half-bright (particle-depleted) scale (SDP). We further modeled the dynamics of the transformation from SDP to LDP upon applying the upward $\mathbf{H}_\mathrm{r}$ with the calculated evolving concentration profiles of the nanoparticles shown in Figure 3b. According to the predictions, the nanoparticles gradually migrated from the pillar base to the tip and the concentration profile first transitioned back from SDP to UP (a constant of 15 vol %) and then gradually transitioned to LDP (a continuous increase from 0 vol % at the pillar base to over 60 vol % at the tip). The whole transition process from SDP to LDP took around 40 s after applying the $\mathbf{H}_\mathrm{r}$. These spatial and temporal variations of the nanoparticle distribution again agreed qualitatively with our experimental observations (insets in Figure 3b and Movie S5), where the particle-enriched base in SDP gradually diffused out to the whole pillar and then migrated and concentrated to the tip region in LDP.

After the nanoparticles were concentrated to either end (base or tip region) of the micropillar, it was interesting to find out whether the redistributed status of the particles could be maintained if the $\mathbf{H}_\mathrm{r}$ was removed. We therefore performed both experimental observations and theoretical predictions on the long-term distributions of the nanoparticles inside the LDP after removing the $\mathbf{H}_\mathrm{r}$. As the results show in Figure 3b (the right-most inset and the blue line), the concentration profile of the nanoparticles at 2 h after removing the $\mathbf{H}_\mathrm{r}$ was nearly the same as that at 40 s after applying the $\mathbf{H}_\mathrm{r}$, indicating that the spontaneous movements (*i.e.*, without magnetic driving) of the particles caused by thermodynamic and possible gravitational effects were not strong enough to alter the spatial distribution of the particles inside the viscous resin adopted here. The redistribution of the particles could thus be temporarily maintained until another external $\mathbf{H}_\mathrm{r}$ was applied. For the transformations from UP to LDP and from LDP to SDP, the scenarios of the evolution kinetics were similar to those reported above except that the directions of the particle migrations were reversed compared to the transformations from UP to SDP and from SDP to LDP, respectively. It should be noted that the interactions between the nanoparticles were neglected in our theoretical models for predicting the evolving concentration profiles. The predicted results should thus deviate from the actual physical processes where the interactions would limit the accumulation velocity and the steric occupancy of the nanoparticles to some extent.[61] Quantitative comparisons between the predictions and the experiments were not achieved in the present study due to the difficulties in measuring the local concentrations of the particles inside the resin channels. However, the combination of the theoretical predictions and experimental observations adequately captured the essences of the magnetophoresis processes and validated the easy and relatively fast modulations of the nanoparticle redistributions for the core−shell magnetic micropillars.

With the concentration profiles of the nanoparticles and the mechanical and geometrical parameters of the redistributed micropillars, we were able to calculate the actuation forces upon applying the horizontal $\mathbf{H}_\mathrm{a}$ and then derive the analytical expressions for the actuated bending deformations. According to the calculations (Figure S5, Supporting Information), the actuation force along the horizontal direction (F_a) dominating the bending deformations continuously decreased from a maximum of ~0.13 N m^{-1} at the pillar base (particle-enriched) to 0 at the middle section (particle-depleted) and then maintained at 0 spanning the middle to the pillar tip for the SDP under the H_a of 350 mT and 25 mT/mm. For the LDP, a reversed trend of the F_a that decreased from the pillar tip to the base was obtained (Figure S5, Supporting Information). These distributions of the F_a were consistent with those of the nanoparticle concentration within the resin channels. In order to derive the analytical solutions of the actuated bending deformations for the SDP and LDP, we simplified the mechanical models by assuming piecewise linear distributions of the F_a along the micropillars and neglecting the contribution of the inside nanocomposite resin to the overall stiffness of the core−shell micropillars (Figure S6, Supporting Information). Such an assumption of the force distributions was made based on our previous study where the theoretically predicted bending deformations using the linear actuation forces agreed well with the experimental ones.[14] To this end, we considered a uniform hollow circular beam subjected to two reversed distributed forces from the side (Figure S6, Supporting Information) and derived the respective deflection curves based on Timoshenko's beam theory (see details for the derivations in the Theories and Computations, Supporting Information).[62] The bending angle (θ_b) as defined in the top inset of Figure 3c, which was used to quantify the actuated bending deformations, was then derived as

https://dx.doi.org/10.1021/acsnano.0c09298
ACS Nano 2021, 15, 4747−4758

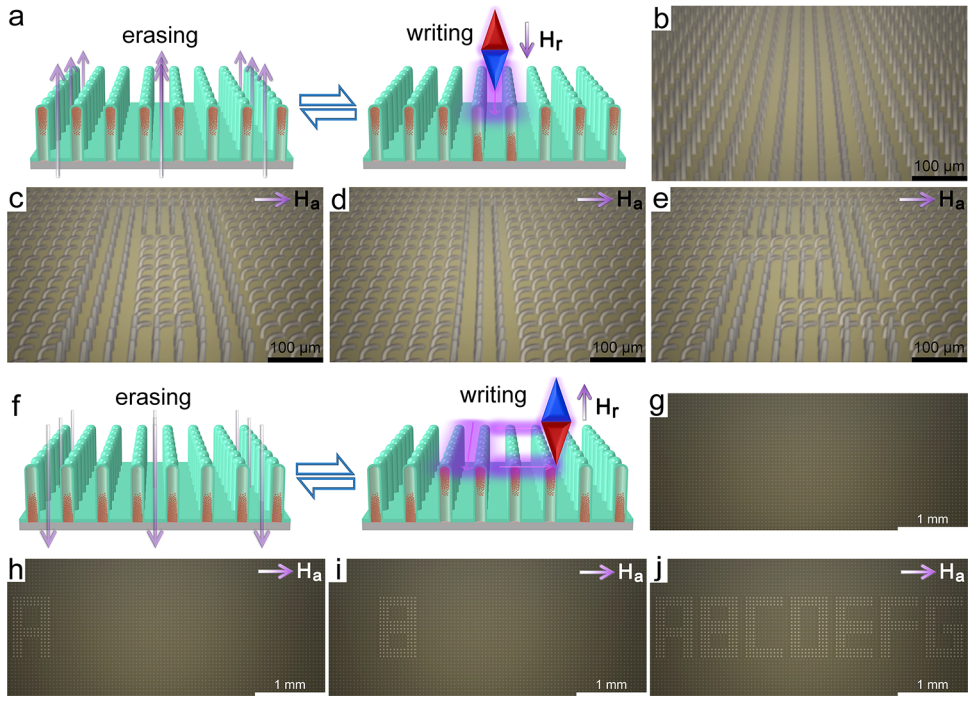

Figure 4. Demonstration of the core−shell magnetic micropillars applied for microscale rewritable paper and recyclable display. (a and f) Schematic diagrams showing the working mechanisms for the magnetic erasing and writing: by applying a global magnetic field (left), all the micropillars are initialized (erased) to the same SDP or LDP state; by approaching and slowly writing on the erased array with a thin magnetic needle (right), the state of the micropillars underneath the written regions is reversed and thus the specific written pattern appears upon actuation. Short arrows indicate the direction of the local redistribution field. Purple-shaded regions indicate the trajectory of the writing. (b and g) Optical microscope images of an erased core−shell magnetic micropillar array from the side view (b) and top view (g). (c−e) Side-view images of the actuated micropillar array after repeatedly erasing and writing with different Arabic numeral patterns from "0" to "9" at the same location (see Figure S10, Supporting Information, for the rest of the numbers). For a movie of the actuations with different numeral patterns see Movie S9. (h−j) Top-view images of the actuated pillar array after repeatedly erasing and writing with different English letters from "A" to "G" at sequential locations (see Figure S11, Supporting Information, for the rest of the letters). Movies S10 and S11 show the actuations and displays of the different written letters. Short arrows indicate the direction of the actuation fields.

$$\theta_b(\mathrm{SDP}) = \frac{q{x_0}^2}{6\kappa GAl} + \frac{q{x_0}^3(l - x_0)}{24EIl} + \frac{q{x_0}^4}{30EIl} \quad (3)$$

$$\theta_b(\mathrm{LDP}) = \frac{q(2l^2 - lx_0 - {x_0}^2)}{6\kappa GAl} + \frac{q{x_0}^4(5l - x_0)}{120EIl(l - x_0)} + \frac{ql^3(11l - 15x_0)}{120EI(l - x_0)} \quad (4)$$

where q is the maximum distribution force per unit length, l is the total length of the micropillar, and x_0 is the distance from the pillar base to the middle point where the actuation force decreases to 0. κ is the shear coefficient for the Timoshenko beam, which can be calculated as $\kappa = \frac{6(1+\nu)(1+\lambda^2)^2}{(7+6\nu)(1+\lambda^2)^2 + (20+12\nu)\lambda^2}$ for the hollow circle section here where ν is the Poisson's ratio of the pillar material and λ is the ratio of the inner radius r to the outer radius R of the hollow beam,[63] G is the shear modulus, E is the elastic modulus of the pillar material, $A = \pi(R^2 - r^2)$ is the area of the cross section, and $I = \frac{\pi}{4}(R^4 - r^4)$ is the moment of inertia of the micropillar.

Based on eqs 3 and 4, the correlations between the pillar geometries and the bending angles can be easily predicted. By adapting the specific parameters from both experiments and calculations (Table S2, Supporting Information) into the equations, we obtained the theoretical predictions of the bending angles for the SDP and LDP under various actuation fields and compared them with the results achieved from experimental observations. As shown in Figure 3c, θ_b increased monotonically with the increase of the actuation field H_a within the field and gradient ranges applied (~50 to ~350 mT and ~5 to ~25 mT/mm) for both the SDP and LDP. However, the rate of the increase differed significantly for these two micropillars with contrasting nanoparticle distributions: the observed θ_b increased from ~1.2° to only ~5° for the SDP, while from ~6.5° to a large bending angle of ~45.5° for the LDP as the H_a increased from 50 mT, 5 mT/mm to 350 mT, 25 mT/mm, in general agreement with the results obtained by simplified finite element analysis shown in Figure S7, Supporting Information. Therefore, by simply modulating the spatial distribution of the magnetic nanoparticles (effectively the actuation force) from the base region to the tip region, the actuated bending deformation (in terms of the bending angle) under the field of 350 mT and 25 mT/mm was tuned by nearly 1 order of magnitude for the core−shell magnetic micropillars. When comparing the experimental results with the theoretical ones, good agreements were obtained for the SDP, while the theories slightly overestimated the actual bending angles for the LDP and the deviation increased with the increase of the actuation field (a deviation of ~5° at the maximum field). Such deviations should be mainly attributed to the simplified linear distributions of the actuation forces and the neglected contribution of the nanocomposite resin channel to the overall bending deformation of the micropillars adopted in the

https://dx.doi.org/10.1021/acsnano.0c09298
ACS Nano 2021, 15, 4747−4758

derivations. We further tested the repeatability of the bending actuation for the LDP by periodically applying and removing the actuation field (350 mT, 25 mT/mm) and measuring the θ_b as a function of the repeating cycle. As the results show in Figure S8, Supporting Information, θ_b degraded very slightly upon applying the H_a within the 50 cycles tested and returned to ∼0° each time the H_a was removed, indicating the good reversibility and repeatability of the actuation performances of the core−shell micropillars. We note that 50 cycles are not enough to demonstrate the long-term durability and ultimate lifetime for the micropillar actuators. A systematic study on the durability and fatigue performances of the micropillars is currently underway and will be presented separately.

Demonstration of the Core−Shell Magnetic Micropillars for Microscale Rewritable Paper and Recyclable Display. Combining the easy modulation of the nanoparticle redistributions and the good controllability of the actuated bending deformations, the core−shell magnetic micropillars presented reprogrammable and reconfigurable actuation capabilities that facilitated potential applications for erasable and rewritable papers as well as recyclable displays. As shown in Figure 4a for the schematic diagrams of the magnetic writing and erasing on the micropillar array, by applying a global upward redistribution field $\mathbf{H}_r$ (left), all the micropillars were initialized to the same LDP state with the inside nanoparticles concentrated at the tip regions. Subsequently, a local downward redistribution field $\mathbf{H}_r$ was applied to selected regions of the array and changed the nanoparticle distribution to the base regions (SDP state) within the locally selective pillars (Figure 4a, right). This was realized by approaching a thin magnetic needle (Figure S9, Supporting Information) to the pillar array and then slowly moving (writing) the needle along a predesigned path above the array (see details in the Experimental Section). In doing so, only the micropillars covered under the written paths were transformed into the SDP, and the rest of the pillars remained in the LDP state. Upon applying a horizontal actuation field $\mathbf{H}_a$, all the SDP remained almost upright, while all the LDP bent over to a large extent (see Movies S7 and S8 for the demonstrations of representative hybrid actuations), a combination of which would make the written paths (SDP regions) visually and structurally exposed by the contrasting bending responses. The exposed paths could be easily erased by reapplying the global $\mathbf{H}_r$ (Figure 4a, left) and then rewritten by applying another local $\mathbf{H}_r$ with a different moving path. These erasing and writing processes could be recycled for infinite times, and therefore various different patterns could be controlled to appear and disappear using the same micropillar array by alternately applying the $\mathbf{H}_r$ and $\mathbf{H}_a$.

On the basis of these concepts of the magnetic writing and erasing, we designed and demonstrated a rewritable magnetic paper that was dynamically written with the Arabic numbers from "0" to "9" as shown in Figure 4b−e, Figure S10, and Movie S9, Supporting Information. Using a single core−shell magnetic micropillar array, we wrote the series of numbers on the same location of the array after each time of erasing. Therefore, the microscale numbers could be controlled to appear upon applying the actuation field and disappear after the field was removed in sequence at the same location of the array (Movie S9). In the present study, the process of the erasing took around 40 s to finish (that was the duration for the complete migration of the nanoparticles from the base region to the tip region inside the resin channels), while that of the writing took several minutes due to the continuous movement of the local redistribution field (*i.e.*, the magnetic needle) with a low velocity of 2 μm/s adopted. These durations could be tuned by adjusting such parameters as the intensity of the redistribution field, the viscosity of the resin, and the magnetization and size of the magnetic nanoparticles. The response time for the bending actuation of the micropillars depended on the speed of the actuation field applied, *i.e.*, the velocity of the actuation magnet approaching the pillar array (Figure S2, Supporting Information). For a velocity of 10 mm/s adopted in the present study, it took only a few seconds to complete a cycle of the appearance and disappearance of one number pattern (Movie S9). The erasable and rewritable paper with a feature size of tens of microns enabled by the reprogrammability of the core−shell magnetic micropillars could be applicable to many practices, including encryptable information storage, recyclable braille printing, anticounterfeiting, dynamic camouflage, and so on.[12−15,30,64,65]

Similar to the working mechanisms of the rewritable paper above, we further demonstrated the reprogrammability of the magnetic micropillar array for potential application to microscale recyclable display (Figure 4f). In contrast to the magnetic writing and erasing adopted in the rewritable paper, we first applied a global downward $\mathbf{H}_r$ to the whole array to initiate all the micropillars to the SDP state (Figure 4f, left). A local upward $\mathbf{H}_r$ was then applied to selected regions of the array to transform the magnetically exposed micropillars to the LDP state (Figure 4f, right). This was realized by reversing the magnetic poles of the magnetic needle to drive the nanoparticles toward the tip regions of the exposed micropillars and then writing on top of the array along a predesigned path. As such, the written micropillars would generate large bending deformations and gradually show the exposed path, while the rest of the pillars remained almost undeformed upon applying the actuation field $\mathbf{H}_a$. The written pattern of the micropillars could also be repeatedly erased by reapplying the global downward $\mathbf{H}_r$ and then adapted to a new configuration by rewriting with a new local upward $\mathbf{H}_r$. By modifying the tips of the micropillars with a dark ink, the whole micropillar array presented a uniform gray color throughout before applying the $\mathbf{H}_a$ (Figure 4g). The pillar array was then written with various English letters from "A" to "G" at sequential locations (from left to right) of the array after each time of erasing. Upon periodically applying and removing the $\mathbf{H}_a$, the series of the letters were controlled to dynamically and sequentially be displayed and concealed at different locations of the array *via* the contrasting bending responses of the exposed LDP and unexposed SDP (Figure 4h,i, Figure S11, and Movie S10, Supporting Information). The series of letters were also demonstrated to be written together on the array such that the combination of the letters was controlled to be displayed and concealed as demanded (Figure 4j and Movie S11).

Extended Discussion and Limitation of the Core−Shell Magnetic Micropillars. As demonstrated above, the core−shell magnetic micropillars present excellent programmability and reprogrammability in the actuation performances thanks to the easy and recyclable modulations of the spatial distribution of the actuating media within the pillars. For the programmable actuation, the micropillars can be controlled to bend to desired configurations by tuning the spatial distribution of the magnetic nanoparticles inside the resin channels of the pillars and/or by adjusting the intensity of the

https://dx.doi.org/10.1021/acsnano.0c09298
ACS Nano 2021, 15, 4747−4758

actuation field. The bending actuations can also be programmed to exert at specified locations of the pillar array with specified patterns by globally and locally modulating the nanoparticle distributions, while for the reprogrammable actuation the individual micropillars can be dynamically switched between SDP and LDP by remodulating the nanoparticle redistributions. As a result, any desired patterns consisting of the deformed LDP and undeformed SDP can be repeatedly achieved at any desired locations using one single micropillar array. These advanced controls with little requirement on the actuation setup enable a spectrum of unusual functionalities and potential applications for the magnetic micropillar array, as demonstrated here for the rewritable paper and recyclable display at the micrometer scale. The simultaneously programmable and reprogrammable actuation capabilities of the core−shell micropillars have not been realized using traditional magnetic micropillars or any other types of stimuli-responsive microstructures,[3,10−12,14,16−21,25,30,33,43,45−50] where the actuated configurations are usually fixed and cannot be easily readapted.

In the present study, the geometries of the core−shell micropillars (pillar diameter, height, shell thickness, and interpillar space) and the materials selections (solidified PUA shells and PUA/Fe_3O_4@SiO_2 nanocomposite resin cores) have been optimized to achieve desired bending actuations while maintaining the structural stability of the pillar array. Such geometrical optimizations are performed based on a previous theoretical model predicting the critical slenderness ratio for lateral collapse of the micropillar array[66] and then considering the combination of the fabrication processability, the structural stability, and the magnetic responsivity of the micropillars. As such, the core−shell micropillars can be reversibly deformed to a large extent (bending angle of ∼45.5° in LDP) for tens of cycles without significantly degrading the structural integrity. The viscosity of the liquid resin cores has also been carefully chosen such that the spatial distribution of the magnetic nanoparticles inside can be easily modulated within a reasonable amount of time and the redistributed status can be maintained for a long duration after removing the modulation field. For the rewritable paper and recyclable display demonstrated, we note that the speeds for the magnetic erasing and writing (usually at the scale of a few minutes) are currently not fast enough comparing with our daily pen-writing and existing display techniques, due to the slow movement and relatively low magnetic field of the magnetic needle adopted during the writings. This limit in the writing speed, however, may be addressed by accelerating the nanoparticle redistributions inside the resin channels: for example, by adopting a magnetic needle with higher local field at the tips, by lowering the viscosity of the resin liquid, and/or by replacing the Fe_3O_4 nanoparticles with other types of magnetic media with higher magnetic responsivity. We also note that the spatial resolution of the core−shell micropillars fabricated here is ∼10 μm and the feature size of a stroke in the writings is limited to ∼100 μm. Attempts in further reducing the sizes of the pillars and the strokes have failed due to the difficulties in balancing the magnetic responsivity and the structural stability of the pillar array. Nevertheless, the concept of the liquid-core/solid-shell magnetic micropillars and the superior reprogrammability endowed will guide future designs and optimizations of reprogrammable responsive micro/nanostructures with higher spatial resolutions and even more attractive performances.

CONCLUSIONS

In summary, we have proposed a concept and developed a corresponding experimental technique for liquid-core/solid-shell magnetic micropillars enabling thus-far-inaccessible reprogrammable actuations. By encapsulating elastomer pillared hollow shells with liquid magnetic nanocomposite resins, the core−shell micropillars can be actuated to contrasting bent configurations (bending angle spanning from ∼5° to ∼45.5°) under the same actuation field, depending on the spatial distribution of the magnetic nanoparticles inside the liquid resin channels. The different bending deformations, as validated by the classical beam theories, can be dynamically achieved through recurrent magnetophoresis processes that locally modulate the nanoparticle redistributions. Therefore, various arbitrary patterns of the micropillars are achieved by direct magnetic writing, and the written patterns are then easily erased and reconfigured by periodically applying global and local redistribution fields. The reprogrammable actuation of the micropillars endows functionalities that facilitate intriguing potential applications, as demonstrated here for the rewritable paper and recyclable display where various microscale characters can be controlled to dynamically appear and disappear at the same or different locations of one single micropillar array. The concept of "actuating in liquid" and the manufacturing technique for the core−shell magnetic micropillars reported here may be extended to other stimuli-responsive systems for both programmable and reprogrammable actuation performances that should find wide applications in various other fields including information encoding,[12,13,64] dynamic sensors and actuators,[25,26,35,43] reconfigurable metasurfaces,[5,16,24] reprogrammable soft robotics,[67,68] *etc.*

EXPERIMENTAL SECTION

Materials. The UV-curable polyurethane acrylate resins used for the solid shells (elastic modulus of ∼8 MPa) were purchased from Minuta Technology Co. Ltd., Korea. The uncurable PUA resins without adding photoinitiators used as the liquid fillings (viscosity of ∼0.16 Pa·s) were purchased from Sigma-Aldrich (Shanghai) Trading Co. Ltd., China. The elastic modulus of the cured PUA and the viscosity of the uncured resin were obtained by quasi-static nanoindentation tests (TI 950, Hysitron Inc., USA) and viscometer measurements (ViscoQC 100L, Anton Paar Shanghai, China), respectively.[14,51] Dispersed Fe_3O_4 nanoparticles (average diameter of ∼20 nm, oleate-stabilized in cyclohexane) were purchased from Nanjing XFNANO Materials Tech. Co., Ltd., China. Tetraethyl orthosilicate (TEOS) for silica coating, PET thin film for sealing and backing, and other assistant reagents used during the sample preparations were all purchased from Sigma-Aldrich, USA. Superhydrophobic spray (Glaco Mirror Coat Zero) for surface treatments was purchased from Soft 99 Ltd., Japan. The silicon negative master with patterned cavities (diameter of 10 μm, depth of 80 μm, and intercavity distance of 40 μm) was obtained by using a typical plasma etching technique[69] while the silicon positive micropillar die (diameter of 6 μm, height of 80 μm, and interpillar distance of 40 μm) was prepared by photolithography combined with deep reactive-ion etching as detailed in the literature.[70] Disk-shaped permanent NdFeB magnets (diameter of 60 mm, height of 5 mm, saturation magnetization of ∼1.3 T, Figure S1) for global nanoparticle redistributions and also actuations were purchased from Supremagnete, Germany. The NdFeB magnetic needle (symmetric cone shape with cone angles of 30°, radius of curvature of the tips of ∼100 μm, total length of 37 mm, Figure S9) for local nanoparticle redistributions (magnetic writings) was customized from Chengdu Amoeba Magnetic Co., Ltd., China.

https://dx.doi.org/10.1021/acsnano.0c09298
ACS Nano 2021, 15, 4747−4758

The cavities of the silicon negative master and the micropillars of the positive die were pretreated in oxygen plasma followed by silanizations to reduce the surface adhesion and facilitate the subsequent peeling-off of the die and the magnetic micropillars during the fabrication of the core−shell micropillars as detailed below.[70] The superparamagnetic Fe_3O_4 nanoparticles were first coated with silica shells (total diameter of ∼30 nm) through a combination of ligand exchange and modified Stöber method as detailed elsewhere.[71] The obtained Fe_3O_4@SiO_2 core−shell nanoparticles were then mixed with the uncurable PUA resin at a ratio of 15 vol % (∼29.5 wt %) to prepare the PUA/Fe_3O_4@SiO_2 nanocomposite resins. The mixing process was carried out by mechanically stirring the mixture overnight and subsequently thoroughly blending in a centrifugal mixer (DAC 150.1 FVZ-K, Hauschild & CoKG, Germany) at 2000 rpm for 1 h. The dispersed nanocomposite mixture was degassed for a few hours and used for the fabrication of the core−shell magnetic micropillars.

Fabrication of the Core−Shell Magnetic Micropillars. The core−shell magnetic micropillars were fabricated by a two-step template casting technique that mainly consisted of the preparation of the solid hollow shells and the subsequent filling-in of the liquid magnetic nanocomposite resin cores, as shown schematically in Figure 1. The UV-curable PUA resins were first drop-dispensed onto the silicon master and infiltrated into the cavities through a vacuum-assisted capillary filling process (step 1, Figure 1). The filling-in process was finished within a few minutes under the combined effects of the air pressure and the capillary force. After the complete infiltration, the surface-modified silicon micropillar die was moved onto the master and carefully aligned to ensure that the thinner micropillars of the die were exactly centered to the wider cavities of the master (step 2, Figure 1). These positioning and centering were accomplished by premarking the boundaries of the master and the die during the etching and moving the die with a homemade movement system consisting of three high-precision piezo actuators (step resolution of ∼24 nm, LAC10A, Zaber Technologies Inc., Canada) assembled in *XYZ* configuration, assisted with a high-resolution optical microscope (BX51M, Olympus, Japan). The aligned micropillar die was then slowly driven into the infiltrated resin channels using the system until there was a ∼2 μm gap left between the die and the master (step 3, Figure 1). The interpositioned resins were thus squeezed out, and the infiltrated resin channels were hollowed by the solid micropillars. Subsequently, the remaining hollow resins were cured and solidified by applying a sufficient UV irradiation (LZ1-10UA00, LED Engin Inc., USA) of 500 mW/cm^2 for 5 min (step 3, Figure 1). The UV irradiation was controlled by a LabVIEW (National Instrument, USA) program through an LED controller (6340 ComboSource, Arroyo Instrument, USA). By mechanically removing the micropillar die from the solidified resins (step 4, Figure 1), the hollowed PUA shell mold with patterned microcavities supported in the silicon master was obtained (step 5, Figure 1).

Next, the prepared PUA/Fe_3O_4@SiO_2 nanocomposite resins were drop-dispensed onto the solidified PUA shell mold and infiltrated into the cavities through a second vacuum-assisted capillary filling process (step 6, Figure 1). After the complete filling-in, the top surface of the mold was cleaned to remove any excess resins and then covered with a thin PET film (step 7, Figure 1). The bottom surface of the PET film (*i.e.*, the surface that contacted the PUA mold) was pretreated with a strong glue such that the infiltrated nanocomposite resins were fully sealed between the PET backing film and the PUA shell mold. The PET backing film, the PUA shell mold, and the sealed magnetic nanocomposite resins were then peeled off from the silicon master (step 7, Figure 1) to achieve the core−shell magnetic micropillars composed of a solid PUA shell encapsulating the liquid magnetic nanocomposite resins (step 8, Figure 1). The obtained core−shell micropillars were finally treated with a superhydrophobic spray to modify the surface properties and reduce the surface adhesion between adjacent pillars.[30]

Characterizations of the Processing Materials and the Fabricated Core−Shell Magnetic Micropillars. The morphologies of the silicon negative master (Figure 2a), the silicon positive die (Figure 2b), the PUA shell mold (Figure 2c), and the fabricated core−shell micropillars (Figure 2e) were characterized by a field-emission scanning electron microscope (FE-SEM, Sirion 200, FEI, USA) from the cross-sectional views. For the characterizations of the shell mold and the core−shell micropillars, the samples were pretreated with a ∼5 nm thick Pt film through sputter coating. The characterizations of the individual PUA shells (insets in Figure 2c) were realized by precision slicing from the shell array in a focused ion beam (FIB-SEM, Auriga Compact, Zeiss, Germany) system. The morphologies of the dispersed Fe_3O_4@SiO_2 core−shell nanoparticles in the PUA resin (Figure 2d) were examined by a TEM (Jeol EM-2100, Japan). Details regarding the sample preparations for the TEM tests can be found in our previous study.[72] The fabricated core−shell magnetic micropillars were also visualized (Figure 2e) using a polarizing optical microscope (Axio Scope A1, Zeiss, Germany). For the capture of the transformation dynamics and the bending movies of the micropillars upon actuation given in the Supplementary Movies, a high-resolution and high-speed CCD camera (Fastcam SA5, Photron, Japan) was equipped with an optical microscope to record the complete transformation and deformation processes.

Modulation of the Nanoparticle Redistributions inside the Resin Channels of the Core−Shell Magnetic Micropillars. After the core−shell magnetic micropillars were successfully fabricated, the spatial distribution of the magnetic nanoparticles inside the resin channels of the micropillars could be easily and dynamically modulated by applying a redistribution magnetic field ($\mathbf{H}_r$) along the axial direction of the pillars. The $\mathbf{H}_r$ was generated by two disk-shaped NdFeB magnets placed in a parallelly repulsive configuration (Figure S1) with the direction of the field controlled by switching the magnetic poles of the magnets. Such a configuration could significantly increase the magnetic field gradient in-between and thus facilitate the nanoparticle migrations in the resin liquid.[73] The intensity of the $\mathbf{H}_r$ was controlled by adjusting the distance between the two magnets. In the present study, this intermagnet distance was fixed at 10 mm and the core−shell micropillar specimen was attached with either the top or the bottom magnet at the middle region. Since the magnetic moments of the nanoparticles were free to rotate within the viscous resin, the particles would migrate toward the closer magnet, and the redistributions toward different directions (*i.e.*, either the pillar tip or the base) could thus be realized. The magnetic field applied to the micropillars was measured to be ∼200 mT and ∼40 mT/mm (410 hand-held gaussmeter, Lakeshore, USA). Such a field of the $\mathbf{H}_r$ was chosen to match the field generated by the magnetic needle during the magnetic writings. The optical microscope equipped with the high-speed CCD camera was configured at the side of the micropillars to capture the transformation dynamics between the various micropillars. After a complete transformation (*e.g.*, from an SDP to an LDP), the $\mathbf{H}_r$ was removed and the micropillar sample was placed still and observed at intervals to see whether the redistributed state of the nanoparticles was maintained.

Actuation of the Core−Shell Magnetic Micropillars. The bending deformations of the SDP and LDP were actuated using the same magnet as for the modulation of the nanoparticle redistributions. Differently, the magnet was configured perpendicularly to the in-plane direction of the micropillars (Figure S2) such that the horizontal actuation field and the bending deformations could be generated. To implement the actuations, we fixed the core−shell micropillar array sample onto a horizontal stage and placed the magnet vertically to the side of the sample. The magnet was initially placed far away from the sample, and the actuation field ($\mathbf{H}_a$) was applied by gradually approaching the magnet toward the sample and removed by retracting the magnet away from the sample. This was realized by fixing the magnet on a computer-controlled motor near the sample and moving the motor until a maximum field of ∼350 mT and ∼25 mT/mm (corresponding to a minimum magnet−specimen distance of ∼5 mm) was achieved. The variation of the H_a as a function of the magnet−specimen distance was measured by the gaussmeter, based on which the magnetic field gradient was obtained by taking the first-order derivative as the results show together in Figure S2b. As such, the response time for the bending actuations of the micropillars could be

https://dx.doi.org/10.1021/acsnano.0c09298
ACS Nano 2021, 15, 4747−4758

controlled by adjusting the moving velocity of the magnet, and the real-time capturing of the bending deformations from the side could thus be facilitated. For a velocity of 10 mm/s adopted in the present study, a response time of a few seconds was achieved for one cycle of the actuation and deactuation. The bending angles of the different micropillars under various H_a (Figure 3c and Figure S8) were obtained by manually analyzing the captured side-view bent micropillars.

Demonstrations of the Core−Shell Magnetic Micropillar Array for Microscale Rewritable Paper and Recyclable Display. For the demonstration of the rewritable paper, the core−shell magnetic micropillar array was first modulated to a monolithic LDP state by applying a global upward $\mathbf{H}_r$ as detailed above. The magnetic needle with a field of ∼200 mT and gradient of ∼40 mT/mm at the tip regions (Figure S9a) was then configured vertically and used to write on top of the pillar array to locally modulate the nanoparticle redistributions within selected micropillars. This was accomplished by fixing the needle to the high-precision piezo actuator stage (same as that used in the sample fabrications) and then slowly approaching the south pole of the needle toward the top of the micropillar array until the gap in-between decreased to ∼100 μm. The local field generated by the needle tip (an affected area of ∼100 μm according to the calculated field distribution shown in Figure S9b) would drive the nanoparticles within the micropillars underneath the needle to the base regions and consequently turn these pillars into SDP. By continuously moving (writing) the needle along a predesigned path at a low velocity of 2 μm/s, all the micropillars covered by the moving path were modulated to SDP, while the rest of the pillars among the array remained as LDP. The deformations of the micropillar array with different written paths upon actuations and deactuations (Movie S9) were captured using the optical microscope from the size view. Because the viewing angle for the capturing was blocked by the magnetic needle and the movement stage, the gradual appearance of the patterns during the writing processes was not captured and only the bending actuations of micropillars after each writing were included in the captured videos.

For the demonstration of the recyclable display, all the micropillars were pretreated with a dark ink at the tips such that the pillar array presented a uniform gray color from the top view regardless of the spatial distribution of the nanoparticles inside (Figure 4g). Similar to the demonstration of the rewritable paper above, the core−shell magnetic micropillar array was first modulated to a monolithic SDP state by applying a global downward $\mathbf{H}_r$. The magnetic needle was then used to write on top of the pillar array to locally modulate the nanoparticle redistributions within selected micropillars. The north pole of the needle was configured to face toward the pillar tips to drive the nanoparticles from the pillar base regions to the tip regions within the written micropillars and consequently turned these selected pillars into LDP. In the present study, we demonstrated the writing and recyclable display of the English letters from "A" to "G" at sequential locations (from left to right) of one single micropillar array (Figure 4, Figure S11, Movie S10). We also demonstrated the writing and display of a combination of letters from "A" to "G" on the same micropillar array (Figure 4j, Movie S11). The deformations of the micropillar array with different written paths upon actuations and deactuations (Movies S10 and S11) were captured using the optical microscope from the top view.

ASSOCIATED CONTENT

Supporting Information

The Supporting Information is available free of charge at https://pubs.acs.org/doi/10.1021/acsnano.0c09298.

Theoretical predictions of the transformation dynamics; calculations of the magnetic fields and forces; derivations and simulations of the actuated bending deformations; schematic diagrams and photographs of the experimental setups; experimentally measured magnetic fields; calculated magnetic forces, nanoparticle concentration profiles and pillar deformations; parameters adopted for the calculations; other experimental data and images (PDF)

Movie S1. Transformation dynamics of a micropillar transitioning from UP to SDP under an H_r of 200 mT, showing the gradual migration of the nanoparticles from the tip region to the base region inside the micropillar (MP4)

Movie S2. Transformation dynamics of a micropillar transitioning from UP to LDP under an H_r of 200 mT, showing the gradual migration of the nanoparticles from the base region to the tip region inside the micropillar (MP4)

Movie S3. Bending movie of a local SDP array upon approaching and retracting a magnet (MP4)

Movie S4. Bending movie of a local LDP array upon approaching and retracting a magnet (MP4)

Movie S5. Transformation dynamics of a micropillar transitioning from SDP to LDP under an H_r of 200 mT, showing the gradual migration of the nanoparticles from the base region to the tip region inside the micropillar (MP4)

Movie S6. Transformation dynamics of a micropillar transitioning from LDP to SDP under an H_r of 200 mT, showing the gradual migration of the nanoparticles from the tip region to the base region inside the micropillar (MP4)

Movie S7. Demonstration of a local actuation on a hybrid micropillar array consisting of half SDP and half LDP pattern (MP4)

Movie S8. Demonstration of a local actuation on a hybrid micropillar array consisting of alternating SDP and LDP (one SDP by one LDP) pattern (MP4)

Movie S9. Demonstration of the core−shell magnetic micropillar array applied as a rewritable paper (MP4)

Movie S10. Demonstration of the core−shell magnetic micropillar array applied for recyclable displays (MP4)

Movie S11. Demonstration of the recyclable display of a combination of the letters from "A" to "G" using the core−shell magnetic micropillar array (MP4)

AUTHOR INFORMATION

Corresponding Author

Zhengzhi Wang − *Department of Engineering Mechanics, School of Civil Engineering, Wuhan University, Wuhan, Hubei 430072, China;* orcid.org/0000-0001-5699-8330; Email: zhengzhi.wang@whu.edu.cn

Authors

Ke Ni − *Department of Engineering Mechanics, School of Civil Engineering, Wuhan University, Wuhan, Hubei 430072, China*

Qi Peng − *Department of Engineering Mechanics, School of Civil Engineering, Wuhan University, Wuhan, Hubei 430072, China*

Enlai Gao − *Department of Engineering Mechanics, School of Civil Engineering, Wuhan University, Wuhan, Hubei 430072, China;* orcid.org/0000-0003-1960-0260

Kun Wang − *Department of Engineering Mechanics, School of Civil Engineering, Wuhan University, Wuhan, Hubei 430072, China*

https://dx.doi.org/10.1021/acsnano.0c09298
ACS Nano 2021, 15, 4747−4758

Qian Shao − *Department of Engineering Mechanics, School of Civil Engineering, Wuhan University, Wuhan, Hubei 430072, China*

Houbing Huang − *Advanced Research Institute of Multidisciplinary Science, Beijing Institute of Technology, Beijing 100081, China*

Longjian Xue − *School of Power and Mechanical Engineering, The Institute of Technological Science, Wuhan University, Wuhan, Hubei 430072, China;* orcid.org/0000-0001-5512-747X

Complete contact information is available at: https://pubs.acs.org/10.1021/acsnano.0c09298

Author Contributions

#K. Ni, Q. Peng, and E. Gao contributed equally to this work.

Notes

The authors declare no competing financial interest.

ACKNOWLEDGMENTS

This work was supported by the National Natural Science Foundation of China (Grant Nos. 11972264, 11602177, 11702199, and 51972028), the Natural Science Foundation of Hubei Province (Grant No. 2016CFB2418), and the Fundamental Research Funds for the Central Universities. The numerical calculations in this work have been done on the supercomputing system in the Supercomputing Center of Wuhan University.

REFERENCES

(1) Lima, M. D.; Li, N.; de Andrade, M. J.; Fang, S.; Oh, J.; Spinks, G. M.; Kozlov, M. E.; Haines, C. S.; Suh, D.; Foroughi, J.; Kim, S. J.; Chen, Y.; Ware, T.; Shin, M. K.; Machado, L. D.; Fonseca, A. F.; Madden, J. D. W.; Voit, W. E.; Galvao, D. S.; Baughman, R. H. Electrically, Chemically, and Photonically Powered Torsional and Tensile Actuation of Hybrid Carbon Nanotube Yarn Muscles. *Science* **2012**, *338*, 928−932.

(2) Zarzar, L. D.; Aizenberg, J. Stimuli-Responsive Chemomechanical Actuation: A Hybrid Materials Approach. *Acc. Chem. Res.* **2014**, *47*, 530−539.

(3) Lum, G. Z.; Ye, Z.; Dong, X.; Marvi, H.; Erin, O.; Hu, W.; Sitti, M. Shape-Programmable Magnetic Soft Matter. *Proc. Natl. Acad. Sci. U. S. A.* **2016**, *113*, E6007−E6015.

(4) de Espinosa, L. M.; Meesorn, W.; Moatsou, D.; Weder, C. Bioinspired Polymer Systems with Stimuli-Responsive Mechanical Properties. *Chem. Rev.* **2017**, *117*, 12851−12892.

(5) Sun, Q.; Wang, D.; Li, Y.; Zhang, J.; Ye, S.; Cui, J.; Chen, L.; Wang, Z.; Butt, H.-J.; Vollmer, D.; Deng, X. Surface Charge Printing for Programmed Droplet Transport. *Nat. Mater.* **2019**, *18*, 936−941.

(6) Sitti, M.; Wiersma, D. S. Pros and Cons: Magnetic *versus* Optical Microrobots. *Adv. Mater.* **2020**, *32*, 1906766.

(7) Hu, W.; Lum, G. Z.; Mastrangeli, M.; Sitti, M. Small-Scale Soft-Bodied Robot with Multimodal Locomotion. *Nature* **2018**, *554*, 81−85.

(8) Kim, Y.; Parada, G. A.; Liu, S.; Zhao, X. Ferromagnetic Soft Continuum Robots. *Sci. Robot.* **2019**, *4*, No. eaax7329.

(9) Hines, L.; Petersen, K.; Lum, G. Z.; Sitti, M. Soft Actuators for Small-Sacle Robotics. *Adv. Mater.* **2017**, *29*, 1603483.

(10) Ren, Z.; Hu, W.; Dong, X.; Sitti, M. Multi-Functional Soft-Bodied Jellyfish-Like Swimming. *Nat. Commun.* **2019**, *10*, 2703.

(11) Lu, H.; Zhang, M.; Yang, Y.; Huang, Q.; Fukuda, T.; Wang, Z.; Shen, Y. Bioinspired Multilegged Soft Millirobot that Functions in Both Dry and Wet Conditions. *Nat. Commun.* **2018**, *9*, 3944.

(12) Cui, J.; Huang, T. Y.; Luo, Z.; Testa, P.; Gu, H.; Chen, X. Z.; Nelson, B. J.; Heyderman, L. J. Nanomagnetic Encoding of Shape-Morphing Micromachines. *Nature* **2019**, *575*, 164−168.

(13) Li, J.; Kamin, S.; Zheng, G.; Neubrech, F.; Zhang, S.; Liu, N. Addressable Metasurfaces for Dynamic Holography and Optical Information Encryption. *Sci. Adv.* **2018**, *4*, No. eaar6768.

(14) Wang, Z.; Wang, K.; Liang, D.; Yan, L.; Ni, K.; Huang, H.; Li, B.; Guo, Z.; Wang, J.; Ma, X.; Tang, X.; Chen, L.-Q. Hybrid Magnetic Micropillar Arrays for Programmable Actuation. *Adv. Mater.* **2020**, *32*, 2001879.

(15) Yu, C.; Guo, H.; Cui, K.; Li, X.; Ye, Y. N.; Kurokawa, T.; Gong, J. P. Hydrogels as Dynamic Memory with Forgetting Ability. *Proc. Natl. Acad. Sci. U. S. A.* **2020**, *117*, 18962−18968.

(16) Cao, M.; Jin, X.; Peng, Y.; Yu, C.; Li, K.; Liu, K.; Jiang, L. Unidirectional Wetting Properties on Multi-Bioinspired Magneto-controllable Slippery Microcilia. *Adv. Mater.* **2017**, *29*, 1606869.

(17) Drotlef, D. M.; Blümler, P.; Papadopoulos, P.; del Campo, A. Magnetically Actuated Patterns for Bioinspired Reversible Adhesion (Dry and Wet). *Adv. Mater.* **2014**, *26*, 775−779.

(18) Huang, Y.; Stogin, B. B.; Sun, N.; Wang, J.; Yang, S.; Wong, T.-S. A Switchable Cross-Species Liquid Repellent Surface. *Adv. Mater.* **2017**, *29*, 1604641.

(19) Zhu, S.; Bian, Y.; Wu, T.; Chen, C.; Jiao, Y.; Jiang, Z.; Huang, Z.; Li, E.; Li, J.; Chu, J.; Hu, Y.; Wu, D.; Jiang, L. High Performance Bubble Manipulation on Ferrofluid-Infused Laser-Ablated Microstructured Surfaces. *Nano Lett.* **2020**, *20*, 5513−5521.

(20) Dong, Y.; Wang, J.; Guo, X.; Yang, S.; Ozen, M. O.; Chen, P.; Liu, X.; Du, W.; Xiao, F.; Demirci, U.; Liu, B. F. Multi-Stimuli-Responsive Programmable Biomimetic Actuator. *Nat. Commun.* **2019**, *10*, 4087.

(21) Li, R.; Jin, D.; Pan, D.; Ji, S.; Xin, C.; Liu, G.; Fan, S.; Wu, H.; Li, J.; Hu, Y.; Wu, D.; Zhang, L.; Chu, J. Stimuli-Responsive Actuator Fabricated by Dynamic Asymmetric Femtosecond Bessel Beam for *in Situ* Particle and Cell Manipulation. *ACS Nano* **2020**, *14*, 5233−5242.

(22) Ko, H.; Javey, A. Smart Actuators and Adhesives for Reconfigurable Matter. *Acc. Chem. Res.* **2017**, *50*, 691−702.

(23) Li, M.; Wang, X.; Dong, B.; Sitti, M. In-Air Fast Response and High Speed Jumping and Rolling of a Light-Driven Hydrogel Actuator. *Nat. Commun.* **2020**, *11*, 3988.

(24) Higgins, S. G.; Becce, M.; Belessiotis-Richards, A.; Seong, H.; Sero, J. E.; Stevens, M. M. High-Aspect-Ratio Nanostructured Surfaces as Biological Metamaterials. *Adv. Mater.* **2020**, *32*, 1903862.

(25) Sniadecki, N. J.; Anguelouch, A.; Yang, M. T.; Lamb, C. M.; Liu, Z.; Kirschner, S. B.; Liu, Y.; Reich, D. H.; Chen, C. S. Magnetic Microposts as An Approach to Apply Forces to Living Cells. *Proc. Natl. Acad. Sci. U. S. A.* **2007**, *104*, 14553−14558.

(26) Liu, Y.; McGuire, A. F.; Lou, H.-Y.; Li, T. L.; Tok, J. B. H.; Cui, B.; Bao, Z. Soft Conductive Micropillar Electrode Arrays for Biologically Relevant Electrophysiological Recording. *Proc. Natl. Acad. Sci. U. S. A.* **2018**, *115*, 11718−11723.

(27) Xin, C.; Yang, L.; Li, J.; Hu, Y.; Qian, D.; Fan, S.; Hu, K.; Cai, Z.; Wu, H.; Wang, D.; Wu, D.; Chu, J. Conical Hollow Microhelices with Superior Swimming Capabilities for Targeted Cargo Delivery. *Adv. Mater.* **2019**, *31*, 1808226.

(28) Dong, X.; Lum, G. Z.; Hu, W.; Zhang, R.; Ren, Z.; Onck, P. R.; Sitti, M. Bioinspired Cilia Arrays with Programmable Nonreciprocal Motion and Metachronal Coordination. *Sci. Adv.* **2020**, *6*, No. eabc9323.

(29) Xia, X.; Afshar, A.; Yang, H.; Portela, C. M.; Kochmann, D. M.; Leo, C. V. D.; Greer, J. R. Electrochemically Reconfigurable Architected Materials. *Nature* **2019**, *573*, 205−213.

(30) Jiang, S.; Hu, Y.; Wu, H.; Zhang, Y.; Zhang, Y.; Wang, Y.; Zhang, Y.; Zhu, W.; Li, J.; Wu, D.; Chu, J. Multifunctional Janus Microplates Arrays Actuated by Magnetic Fields for Water/Light Switches and Bio-Inspired Assimilatory Coloration. *Adv. Mater.* **2019**, *31*, 1807507.

(31) Wang, C.; Linghu, C.; Nie, S.; Li, C.; Lei, Q.; Tao, X.; Zeng, Y.; Du, Y.; Zhang, S.; Yu, K.; Jin, H.; Chen, W.; Song, J. Programmable and Scalable Transfer Printing with High Reliability and Efficiency for Flexible Inorganic Electronics. *Sci. Adv.* **2020**, *6*, No. eabb2393.

(32) Wang, W.; Timonen, J. V. I.; Carlson, A.; Drotlef, D.-M.; Zhang, C. T.; Kolle, S.; Grinthal, A.; Wong, T.-S.; Hatton, B.; Kang, S.

H.; Kennedy, S.; Chi, J.; Blough, R. T.; Sitti, M.; Mahadevan, L.; Aizenberg, J. Multifunctional Ferrofluid-Infused Surfaces with Reconfigurable Multiscale Topography. *Nature* **2018**, *559*, 77−82.
(33) Yao, Y.; Waters, J. T.; Shneidman, A. V.; Cui, J.; Wang, X.; Mandsberg, N. K.; Li, S.; Balazs, A. C.; Aizenberg, J. Multiresponsive Polymeric Microstructures with Encoded Predetermined and Self-Regulated Deformability. *Proc. Natl. Acad. Sci. U. S. A.* **2018**, *115*, 12950−12955.
(34) Lendlein, A.; Gould, O. E. C. Reprogrammable Recovery and Actuation Behavior of Shape-Memory Polymers. *Nat. Rev. Mater.* **2019**, *4*, 116−133.
(35) Lendlein, A. Fabrication of Reprogrammable Shape-Memory Polymer Actuators for Robotics. *Sci. Robot.* **2018**, *3*, No. eaat9090.
(36) Alapan, Y.; Karacakol, A. C.; Guzelhan, S. N.; Isik, I.; Sitti, M. Reprogrammable Shape Morphing of Magnetic Soft Machines. *Sci. Adv.* **2020**, *6*, No. eabc6414.
(37) Yang, Y.; Terentjev, E. M.; Zhang, Y.; Chen, Q.; Zhao, Y.; Wei, Y.; Ji, Y. Reprocessable Thermoset Soft Actuators. *Angew. Chem., Int. Ed.* **2019**, *58*, 17474−17479.
(38) Ze, Q.; Kuang, X.; Wu, S.; Wong, J.; Montgomery, S. M.; Zhang, R.; Kovitz, J. M.; Yang, F.; Qi, H. J.; Zhao, R. Magnetic Shape Memory Polymers with Integrated Multifunctional Shape Manipulation. *Adv. Mater.* **2020**, *32*, 1906657.
(39) Verpaalen, R. C. P.; da Cunha, M. P.; Engels, T. A. P.; Debije, M. G.; Schenning, A. P. H. J. Liquid Crystal Networks on Thermoplastics: Reprogrammable Photo-Responsive Actuators. *Angew. Chem., Int. Ed.* **2020**, *59*, 4532−4536.
(40) He, Q.; Wang, Z.; Wang, Y.; Minori, A.; Tolley, M. T.; Cai, S. Electrically Controlled Liquid Crystal Elastomer-Based Soft Tubular Actuator with Multimodal Actuation. *Sci. Adv.* **2019**, *5*, No. eaax5746.
(41) Gelebart, A. H.; Mulder, D. J.; Vantomme, G.; Schenning, A. P. H. J.; Broer, D. J. A Rewritable, Reprogrammable, Dual Light-Responsive Polymer Actuator. *Angew. Chem., Int. Ed.* **2017**, *56*, 13436−13439.
(42) Song, H.; Lee, H.; Lee, J.; Choe, J. K.; Lee, S.; Yi, J. Y.; Park, S.; Yoo, J.-W.; Kwon, M. S.; Kim, J. Reprogrammable Ferromagnetic Domains for Reconfigurable Soft Magnetic Actuators. *Nano Lett.* **2020**, *20*, 5185−5192.
(43) Kim, J.; Chuang, S. E.; Choi, S. E.; Lee, H.; Kim, J.; Kwon, S. Programming Magnetic Anisotropy in Polymeric Microactuators. *Nat. Mater.* **2011**, *10*, 747−752.
(44) Wang, L.; Razzaq, M. Y.; Rudolph, T.; Heuchel, M.; Nöchel, U.; Mansfeld, U.; Jiang, Y.; Gould, O. E. C.; Behl, M.; Kratz, K.; Lendlein, A. Reprogrammable, Magnetically Controlled Polymeric Nanocomposite Actuators. *Mater. Horiz.* **2018**, *5*, 861−867.
(45) Lee, K. J.; Yoon, J.; Rahmani, S.; Hwang, S.; Bhaskar, S.; Mitragotri, S.; Lahann, J. Spontaneous Shape Reconfigurations in Multicompartmental Microcylinders. *Proc. Natl. Acad. Sci. U. S. A.* **2012**, *109*, 16057−16062.
(46) Wang, Z.; Wang, K.; Tang, X. Heterogeneous Magnetic Micropillars for Regulated Bending Actuation. *Extreme Mech. Lett.* **2020**, *38*, 100734.
(47) Al-Azawi, A.; Cenev, Z.; Tupasela, T.; Peng, B.; Ikkala, O.; Zhou, Q.; Jokinen, V.; Franssila, S.; Ras, R. H. A. Tunable and Magnetic Thiol-Ene Micropillar Arrays. *Macromol. Rapid Commun.* **2020**, *41*, 1900522.
(48) Jeon, J.; Park, J. E.; Park, S. J.; Won, S.; Zhao, H.; Kim, S.; Shim, B. S.; Urbas, A.; Hart, A. J.; Ku, Z.; Wie, J. J. Shape-Programmed Fabrication and Actuation of Magnetically Active Microdots Arrays. *ACS Appl. Mater. Interfaces* **2020**, *12*, 17113−17120.
(49) Kim, Y.; Yuk, H.; Zhao, R.; Chester, S. A.; Zhao, X. Printing Ferromagnetic Domains for Untethered Fast-Transforming Soft Materials. *Nature* **2018**, *558*, 274−279.
(50) Brisbois, C. A.; Tasinkevych, M.; Vázquez-Montejo, P.; de la Cruz, M. O. Actuation of Magnetoelastic Membranes in Precessing Magnetic Fields. *Proc. Natl. Acad. Sci. U. S. A.* **2019**, *116*, 2500−2505.
(51) Wang, Z.; Shi, X.; Huang, H.; Yao, C.; Xie, W.; Huang, C.; Gu, P.; Ma, X.; Zhang, Z.; Chen, L.-Q. Magnetically Actuated Functional Gradient Nanocomposites for Strong and Ultra-Durable Biomimetic Interfaces/Surfaces. *Mater. Horiz.* **2017**, *4*, 869−877.
(52) Wang, Z. Slanted Functional Gradient Micropillars for Optimal Bioinspired Dry Adhesion. *ACS Nano* **2018**, *12*, 1273−1284.
(53) Erb, R. M.; Libanori, R.; Rothfuchs, N.; Studart, A. R. Composites Reinforced in Three Dimensions by Using Low Magnetic Fields. *Science* **2012**, *335*, 199−204.
(54) Le Ferrand, H.; Bouville, F.; Niebel, T. P.; Studart, A. R. Magnetically Assisted Slip Casting of Bioinspired Heterogeneous Composites. *Nat. Mater.* **2015**, *14*, 1172−1179.
(55) Choi, S. J.; Kim, H. N.; Bae, W. G.; Suh, K. Y. Modulus- and Surface Energy-Tunable Ultraviolet-Curable Polyurethane Acrylate: Properties and Applications. *J. Mater. Chem.* **2011**, *21*, 14325−14335.
(56) Wang, Z. Spatial and Temporal Tunability of Magnetically-Actuated Gradient Nanocomposites. *Soft Matter* **2019**, *15*, 3133−3148.
(57) Furlani, E. P.; Xue, S. Field, Force and Transport Analysis for Magnetic Particle-Based Gene Delivery. *Microfluid. Nanofluid.* **2012**, *13*, 589−602.
(58) Friedman, G.; Yellen, B. Magnetic Separation, Manipulation and Assembly of Solid Phase in Fluids. *Curr. Opin. Colloid Interface Sci.* **2005**, *10*, 158−166.
(59) Chandrasekhar, S. Stochastic Problems in Physics and Astronomy. *Rev. Mod. Phys.* **1943**, *15*, 1−89.
(60) Furlani, E. P.; Ng, K. C. Analytical Model of Magnetic Nanoparticle Transport and Capture in the Microvasculature. *Phys. Rev. E* **2006**, *73*, 061919.
(61) Sun, J.; Shi, Z.; Chen, S.; Jia, S. Experimental and Numerical Analysis of the Magnetophoresis of Magnetic Nanoparticles under the Influence of Cylindrical Permanent Magnet. *J. Magn. Magn. Mater.* **2019**, *475*, 703−714.
(62) Timoshenko, S. P.; Goodier, J. N. *Theory of Elasticity*, 3rd ed.; McGraw-Hill: New York, 1970; pp 41−60.
(63) Hutchinson, J. R. Shear Coefficients for Timoshenko Beam Theory. *J. Appl. Mech.* **2001**, *68*, 87−92.
(64) Li, L.; Cui, T. J.; Ji, W.; Liu, S.; Ding, J.; Wan, X.; Li, Y. B.; Jiang, M.; Qiu, C.-W.; Zhang, S. Electromagnetic Reprogrammable Coding-Metasurface Holograms. *Nat. Commun.* **2017**, *8*, 197.
(65) Deng, J.; Deng, L.; Guan, Z.; Tao, J.; Li, G.; Li, Z.; Li, Z.; Yu, S.; Zheng, G. Multiplexed Anticounterfeiting Meta-Image Displays with Single-Sized Nanostructures. *Nano Lett.* **2020**, *20* (2020), 1830−1838.
(66) Chandra, D.; Yang, S. Stability of High-Aspect-Ratio Micropillar Arrays against Adhesive and Capillary Forces. *Acc. Chem. Res.* **2010**, *43*, 1080−1091.
(67) Rus, D.; Tolley, M. T. Design, Fabrication and Control of Soft Robots. *Nature* **2015**, *521*, 467−475.
(68) Rich, S. I.; Wood, R. J.; Majidi, C. Untethered Soft Robotics. *Nat. Electron.* **2018**, *1*, 102−112.
(69) Elbersen, R.; Vijselaar, W.; Tiggelaar, R. M.; Gardeniers, H.; Huskens, J. Fabrication and Doping Methods for Silicon Nano- and Micropillar Arrays for Solar-Cell Applications: A Review. *Adv. Mater.* **2015**, *27*, 6781−6796.
(70) Jeong, H. E.; Lee, J. K.; Kim, H. N.; Moon, S. H.; Suh, K. Y. A Nontransferring Dry Adhesive with Hierarchical Polymer Nanohairs. *Proc. Natl. Acad. Sci. U. S. A.* **2009**, *106*, 5639−5644.
(71) Rho, W.-Y.; Kim, H. M.; Kyeong, S.; Kang, Y. L.; Kim, D. H.; Kang, H.; Jeong, C.; Kim, D. E.; Lee, Y. S.; Jun, B. H. Facile Synthesis of Monodispersed Silica-Coated Magnetic Nanoparticles. *J. Ind. Eng. Chem.* **2014**, *20*, 2624−2649.
(72) Wang, Z.; Gu, P.; Wu, X. P.; Zhang, H.; Zhang, Z.; Chiang, M. Y. M. Micro/Nano Wear Studies on Epoxy/Silica Nanocomposites. *Compos. Sci. Technol.* **2013**, *79*, 49−57.
(73) Wang, Z.; Wang, K.; Huang, H.; Cui, X.; Shi, X.; Ma, X.; Li, B.; Zhang, Z.; Tang, X.; Chiang, M. Y. M. Bioinspired Wear-Resistant and Ultradurable Functional Gradient Coatings. *Small* **2018**, *14*, 1802717.

https://dx.doi.org/10.1021/acsnano.0c09298
ACS Nano 2021, 15, 4747−4758

Supporting Information

Core-Shell Magnetic Micropillars for Reprogrammable Actuation

Ke Ni[a†], Qi Peng[a†], Enlai Gao[a†], Kun Wang[a], Qian Shao[a], Houbing Huang[b], Longjian Xue[c], Zhengzhi Wang[a*]

[a] Department of Engineering Mechanics, School of Civil Engineering, Wuhan University Wuhan, Hubei 430072, China
[b] Advanced Research Institute of Multidisciplinary Science, Beijing Institute of Technology Beijing 100081, China
[c] School of Power and Mechanical Engineering, The Institute of Technological Science, Wuhan University, Wuhan, Hubei 430072, China
*Corresponding author. E-mail: zhengzhi.wang@whu.edu.cn

This PDF file includes:

Other supplementary materials for this manuscript include the following:

Supplementary Text. Theories and Computations

1. Predictions of the evolving nanoparticle distributions during the modulations

In order to predict the evolution of the nanoparticle redistributions during the modulations, we performed numerical simulations to describe the motions of the nanoparticles under a combination of the thermodynamic fluctuating force $\mathbf{F}_f(t)$, the viscous dragging force $\mathbf{F}_\eta(t)$, and the magnetic driving force $\mathbf{F}_m(\mathbf{r})$. The transport of the nanoparticles in the viscous resin channel was assumed as a Brownian motion process with the evolving particle positions predicted by the Langevin's equation:[1]

$$m\frac{d^2\mathbf{r}}{dt^2} = \mathbf{F}_f(t) + \mathbf{F}_\eta(t) + \mathbf{F}_m(\mathbf{r}) \quad \text{(S1)}$$

where m is the mass of the nanoparticle, $\mathbf{r}$ is the spatial position of the particle within the resin channel, and t is the time. In a system without considering the damping effect, the first term of the force $\mathbf{F}_f(t)$ can be calculated as:

$$\mathbf{F}_f(t) = m\frac{d^2\mathbf{r}}{dt^2} \quad \text{(S2)}$$

where the average value of the fluctuating force in the whole system follows:

$$\left\langle \mathbf{F}_f(t) \right\rangle = 0 \quad \text{(S3)}$$

and

$$\left\langle m\left(\frac{d\mathbf{r}}{dt}\right)^2 \right\rangle = 3k_BT \quad \text{(S4)}$$

where k_B is the Boltzmann constant and T is the absolute temperature.

The second term of the force $\mathbf{F}_\eta(t)$ can be calculated as:

$$\mathbf{F}_\eta(t) = -6\pi\eta R_p\frac{d\boldsymbol{r}}{dt} \quad \text{(S5)}$$

where η is the viscous constant of the resin liquid and R_p is the radius of the nanoparticle.

The third term of the force $\mathbf{F}_m(\mathbf{r})$ can be calculated as:

$$\mathbf{F}_m(\mathbf{r}) = \frac{(\chi_p - \chi_r)V_p(\mathbf{B}\cdot\nabla\mathbf{B})}{\mu_0} \quad \text{(S6)}$$

which is detailed in the main article.

We simulated the motions of 50000 magnetic nanoparticles inside a cylindrical resin channel with 6 μm diameter and 80 μm length and divided the channel into 80 layers. The evolving concentration profiles of the nanoparticles along the resin channels (results shown in Figure 3b and Figure S4) were then obtained by solving the governing equation using the finite difference method and accumulating the number of the particles that reached each layer at each time step. Considering the core-shell structure of the micropillars studied, the elastic scattering boundary conditions were adopted in the calculations.

2. Calculations of the magnetic fields and forces

The magnetic potential $\phi_m(\mathbf{r})$ of a permanent magnet can be calculated by:[2]

$$\phi_m(\mathbf{r}) = \frac{1}{4\pi}\oint_S \frac{\mathbf{M}_{SM}\cdot\mathbf{n}}{D}dS + \frac{1}{4\pi}\int_\tau \frac{\nabla\cdot\mathbf{M}_{SM}}{D}d\tau \quad \text{(S7)}$$

where $\mathbf{M_{SM}}$ is the saturation magnetization of the permanent magnet, $\mathbf{n}$ is the unit of normal vector at the surface of the magnet, D is the distance between the source point and the field point, S is the surface of the permanent magnet, and τ is the volume of the magnet. The magnetic field generated by the magnet can then be calculated as:

$$\mathbf{H} = -\nabla\cdot\phi_m \quad \text{(S8)}$$

where ∇ is the gradient operator. Substituting Equation (S8) into Equation (S7) gives:

$$\mathrm{H} = -\oint_S \frac{\rho_S}{4\pi}\cdot\nabla\frac{1}{D}d\mathrm{S} = \oint_S \frac{\rho_S}{4\pi}\cdot\frac{\mathbf{D}}{D^3}d\mathrm{S} \quad \text{(S9)}$$

where $\rho_S = \mathbf{M}_{SM}\cdot\mathbf{n}$ is the surface charge density. By adapting the specific parameters into Equation (S9), we obtained the magnetic field distributions generated by the disk-shaped magnets adopted for the modulations and actuations, as the results shown in Figures S3. The magnetic forces applied to the micropillars upon actuation (Figure S5) were then calculated by adapting the fields into Equation (S6) and summing up the forces to single nanoparticles at each layer of the micropillars based on the concentration profiles of the nanoparticles obtained by the theoretical predictions.

The magnetic field generated by the symmetrical cone-shaped magnet needle was computed using a finite element model based on the following theories:

$$\begin{cases} \nabla \cdot \left(\mu_0 \mathbf{H} + \mu_0 \mathbf{M}_{SM} \right) = 0 & \text{in magnet} \\ \nabla \cdot \left(\mu_0 \mu_r \mathbf{H} \right) = 0 & \text{in other media} \end{cases}$$

(S10)

where μ_0 is the permeability of the free space and μ_r is the relative magnetic permeability of any media comparing to μ_0. The obtained magnetic flux density distribution in the vicinity of the needle tips is shown in Figure S9.

3. Derivations of the actuated bending deformations for SDP and LDP

In order to derive the analytical solutions of the actuated bending deformations for the SDP and LDP, we simplified the mechanical models by assuming piecewise linear distributions of the actuation forces along the micropillars and neglecting the contribution of the inside liquid nanocomposite resin to the overall stiffness of the core-shell micropillars. Such assumptions were adopted based on the experimental observations shown in Figure 3a and the calculated results of the nanoparticle concentrations shown in Figure 3b, where the nanoparticles were accumulated to the end (either the base or the tip) of the micropillars and became depleted at a postion of ~ 30 μm from the end for both the SDP and LDP. We therefore considered a uniform hollow circular beam subjected to two reversed linearly-distributed forces from the side (Figure S6) and derived the respective deflection curves based on the Timoshenko's beam theory.[3]

For the SDP, the actuation force is assumed to decrease linearly from the maximum distribution force of q per unit volume at $x = 0$ to 0 at $x = x_0$ (Figure S6, left), which can be expressed as:

$$q_{SDP}(x) = \begin{cases} q\dfrac{x_0 - x}{x_0}, & for \;\; 0 \le x \le x_0 \\ 0, & for \;\; x_0 \le x \le l \end{cases}$$

(S11)

where x is the coordinate postion along the axial direction of the pillar and l is the total length of the pillar. The bending moment (M) and the shear stress (Q) along the axial direction of the SDP for $0 \le x \le x_0$ can then be calculated as:

$$\begin{cases} M_{SDP}(x) = -\dfrac{q}{6x_0}(x_0 - x)^3 \\ Q_{SDP}(x) = \dfrac{q}{2x_0}(x_0 - x)^2 \end{cases}$$

(S12)

The bending deflection (δ) of the SDP within the 0 to x_0 section can thus be obtained by solving the Timoshenko's beam theory:[3]

$$\begin{cases} EI\dfrac{d\theta(x)}{dx} = -M(x) \\ \kappa GA\left[\dfrac{d\delta(x)}{dx} - \theta(x)\right] = Q(x) \end{cases}$$

(S13)

where E is the elastic modulus of the pillar material and $I = \frac{\pi}{4}(R^4 - r^4)$ is the moment of inertia of the hollow circular pillar with inner radius of r and outer radius of R, $\theta(x)$ is the slope rotation angle at position x, κ is the shear coefficient for Timoshenko beam which can be calculated as $\kappa = \frac{6(1+\nu)(1+\lambda^2)^2}{(7+6\nu)(1+\lambda^2)^2 + (20+12\nu)\lambda^2}$ for the hollow circle section where ν is the Poisson's ratio of the pillar material and $\lambda = \frac{r}{R}$ is the radius ratio,[4] $G = \frac{E}{2(1+\nu)}$ is the shear modulus of the pillar material, and $A = \pi(R^2 - r^2)$ is the area of the cross section of the pillar.

For the x_0 to l section along the SDP, no actuation force is applied and the deflection can be calculated as:

$$\delta_{SDP}(x) = \delta_{SDP}(x_0) + \theta_{SDP}(x_0)(x - x_0)$$

(S14)

By solving Equation (S13) and then adapting the calculated results into Equation (S14), the bending deflection of the SDP along the whole micropillar can be combined and expressed as:

$$\delta_{SDP}(x) = \begin{cases} \dfrac{q[x_0^3 - (x_0 - x)^3]}{6\kappa GAx_0} + \dfrac{q(x_0 - x)^5}{120x_0EI} + \dfrac{qx_0^3x}{24EI} - \dfrac{qx_0^4}{120EI} & (for\ \ 0 \le x \le x_0) \\ \dfrac{qx_0^2}{6\kappa GA} + \dfrac{qx_0^3(x - x_0)}{24EI} + \dfrac{qx_0^4}{30EI} & (for\ \ x_0 \le x \le l) \end{cases}$$

(S15)

The bending angle at the pillar tip (θ_b) as defined in the top inset of Figure 3c can be derived as:

$$\theta_b(SDP) = \frac{qx_0^2}{6\kappa GAl} + \frac{qx_0^3(l - x_0)}{24EIl} + \frac{qx_0^4}{30EIl}$$

(S16)

- For the LDP, similarly, the actuation force is assumed to increase linearly from 0 at the middle point $x = x_0$ to the maximum q at the tip $x = l$ (Figure S6, right):

$$q_{LDP}(x)=\begin{cases}0, & for\ \ 0\le x\le x_0\\ q\dfrac{x-x_0}{l-x_0}, & for\ \ x_0\le x\le l\end{cases}$$

(S17)

The bending moment and the shear stress along the axial direction of the LDP can then be calculated as:

$$M_{LDP}(x)=\begin{cases}-\dfrac{q(l-x_0)(2l+x_0-3x)}{6}, & for\ \ 0\le x\le x_0\\ -\dfrac{q(l-x)^2(2l+x-3x_0)}{6(l-x_0)}, & for\ \ x_0\le x\le l\end{cases}$$

(S18)

$$Q_{LDP}(x)=\begin{cases}\dfrac{q(l-x_0)}{2}, & for\ \ 0\le x\le x_0\\ \dfrac{q(l-x)(l+x-2x_0)}{2(l-x_0)}, & for\ \ x_0\le x\le l\end{cases}$$

(S19)

The bending deflection of the LDP within the 0 to x_0 section can be obtained by solving the same Timoshenko's beam theory given in Equation (S13):

$$\delta_{LDP}(x)=\frac{q(l-x_0)x}{2\kappa GA}+\frac{q(l-x_0)x^2(2l+x_0-x)}{12EI}$$

(S20)

Similarly, the bending deflection of the LDP within the x_0 to l section can be obtained by solving Equation (S13) and taking the boundary conditions:

$$\begin{cases}\delta_{LDP}\big|_{x=x_0}=\delta_{LDP}(x_0)\\ \theta_{LDP}\big|_{x=x_0}=\theta_{LDP}(x_0)\end{cases}$$

(S21)

The bending deflection of the LDP along the whole micropillar can be combined and expressed as:

$$\delta_{LDP}(x)=\begin{cases}\dfrac{q(l-x_0)x}{2\kappa GA}+\dfrac{q(l-x_0)x^2(2l+x_0-x)}{12E_0I} & \left(for\ \ 0\le x\le x_0\right)\\ \dfrac{q(3l^2x-x^3-6lx_0x+3x^2x_0+{x_0}^3)}{6\kappa GA(l-x_0)}+\dfrac{q{x_0}^4x}{24E_0I(l-x_0)}-\dfrac{q{x_0}^5}{120E_0I(l-x_0)} & \\ +\dfrac{qx^2}{120E_0I(l-x_0)}[20l^3-10l^2(x+3x_0)+20lxx_0+x^2(x-5x_0)]\ \left(for\ \ x_0\le x\le l\right) & \end{cases}$$

(S22)

The bending angle at the pillar tip is then derived as:

$$\theta_b(LDP) = \frac{q(2l^2 - lx_0 - x_0^2)}{6\kappa GAl} + \frac{qx_0^4(5l - x_0)}{120EIl(l - x_0)} + \frac{ql^3(11l - 15x_0)}{120EI(l - x_0)}$$

(S23)

4. Finite element analysis of the actuated bending deformations for SDP and LDP

The actuated bending deformations for SDP and LDP were calculated by conducting a series of simplified finite element analyses. To this end, we established a three-dimensional numerical model that considered the core-shell micropillar as a uniform hollow cylinder (inner diameter of 6 μm, outer diameter of 10 μm, height of 80 μm), where the contribution of the inside liquid nanocomposite resin to the overall stiffness was neglected. The actuation forces were applied on the micropillars as linearly-distributed edge loadings within a length range of 30 μm (Figure S6), and the bottom end of the micropillar was fixed. The domain was discretized with 5229 tetrahedral elements. Considering the large deformations of the micropillars, the geometric nonlinearity was included in the calculations. The resulted bending deformations for SDP and LDP subjected to various actuation forces are shown in Figure S7. The colored contours which denote the horizontal deflections (δ) for SDP and LDP reveal that the maximum deflection for LDP is ~50 μm (in case of H_a = 350 mT), while that for SDP is less than 5 μm.

It should be noted that the finite element analyses presented here were intended to corroborate and interpret the mechanistic mechanisms for the contrasting bending behaviors of the SDP and LDP. Therefore, simplified loading conditions (*i.e.* constant piecewise linear distribution forces) and materials parameters (linear elasticity) were adopted and quantitative comparisons between the experiments and simulations are not expected.

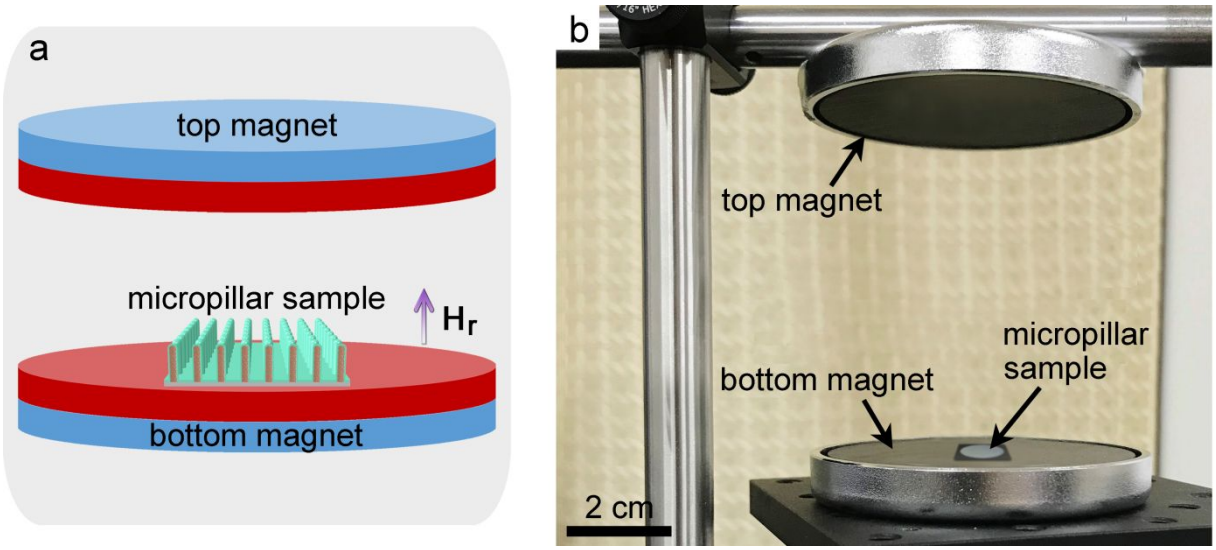

Figure S1. (a) Schematic diagram and (b) photograph of the redistribution magnetic field ($\mathbf{H_r}$) setup for the nanoparticle modulations of the micropillars.

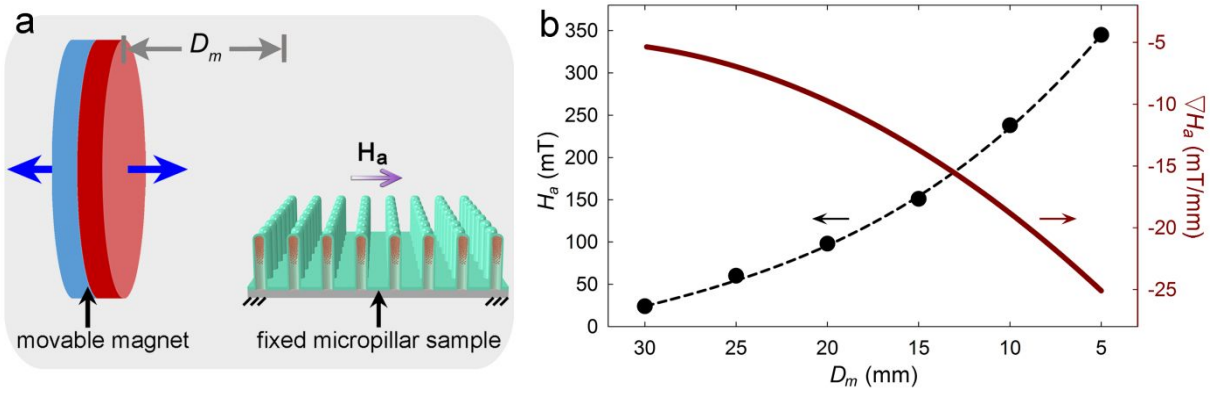

Figure S2. (a) Schematic diagram of the experimental setup for the micropillar actuation. (b) measured actuation field (H_a) and calculated field gradient (∇H_a) as a function of the magnet-sample distance (D_m), the dashed line is obtained by curve-fitting on the discrete experimental data using a cubic polynomial function while the solid line is obtained by taking the first-order derivative of the curve-fitted function.

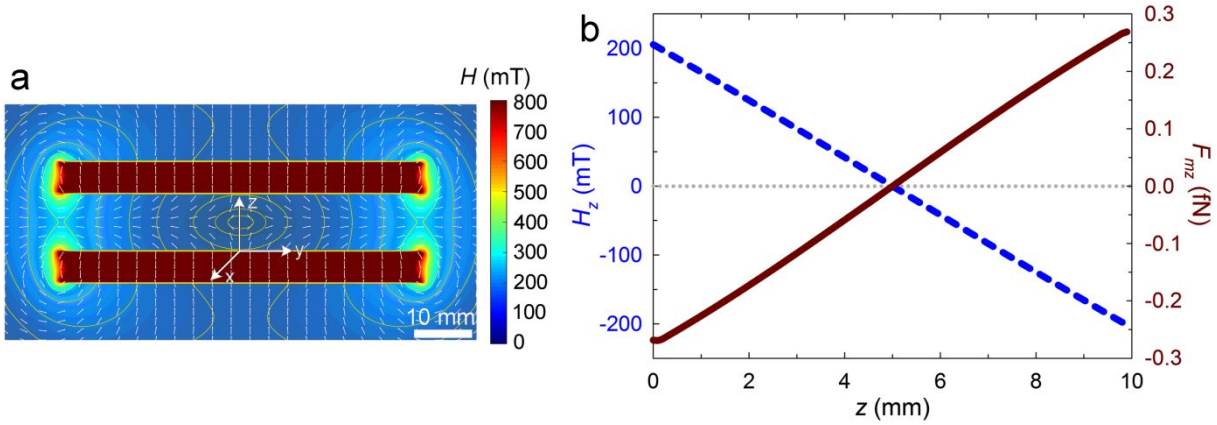

Figure S3. (a) Calculated magnet field distribution of two magnets placed in repulsion configuration at an inter-magnet distance of 10 mm as adopted in the experiments for the global nanoparticle modulations. (b) Magnetic field (H_z) and force to a single nanoparticle (F_{mz}) along the axial direction of the micropillar (*i.e.* the z direction shown here) as a function of the z distance above the top of the bottom magnet where the micropillar sample is placed during the modulations.

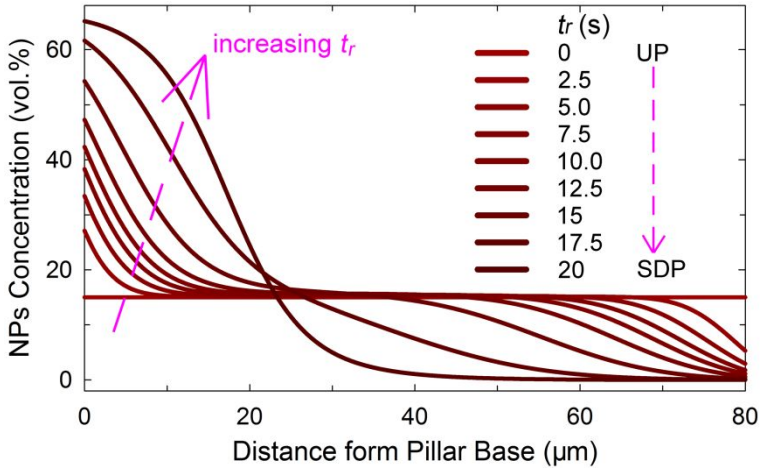

Figure S4. Theoretical predictions of the nanoparticle concentration distribution along the resin channel at various times (t_r) after applying a downward H_r of 200 mT and 40 mT/mm on a UP (*i.e.* transformation from UP to SDP).

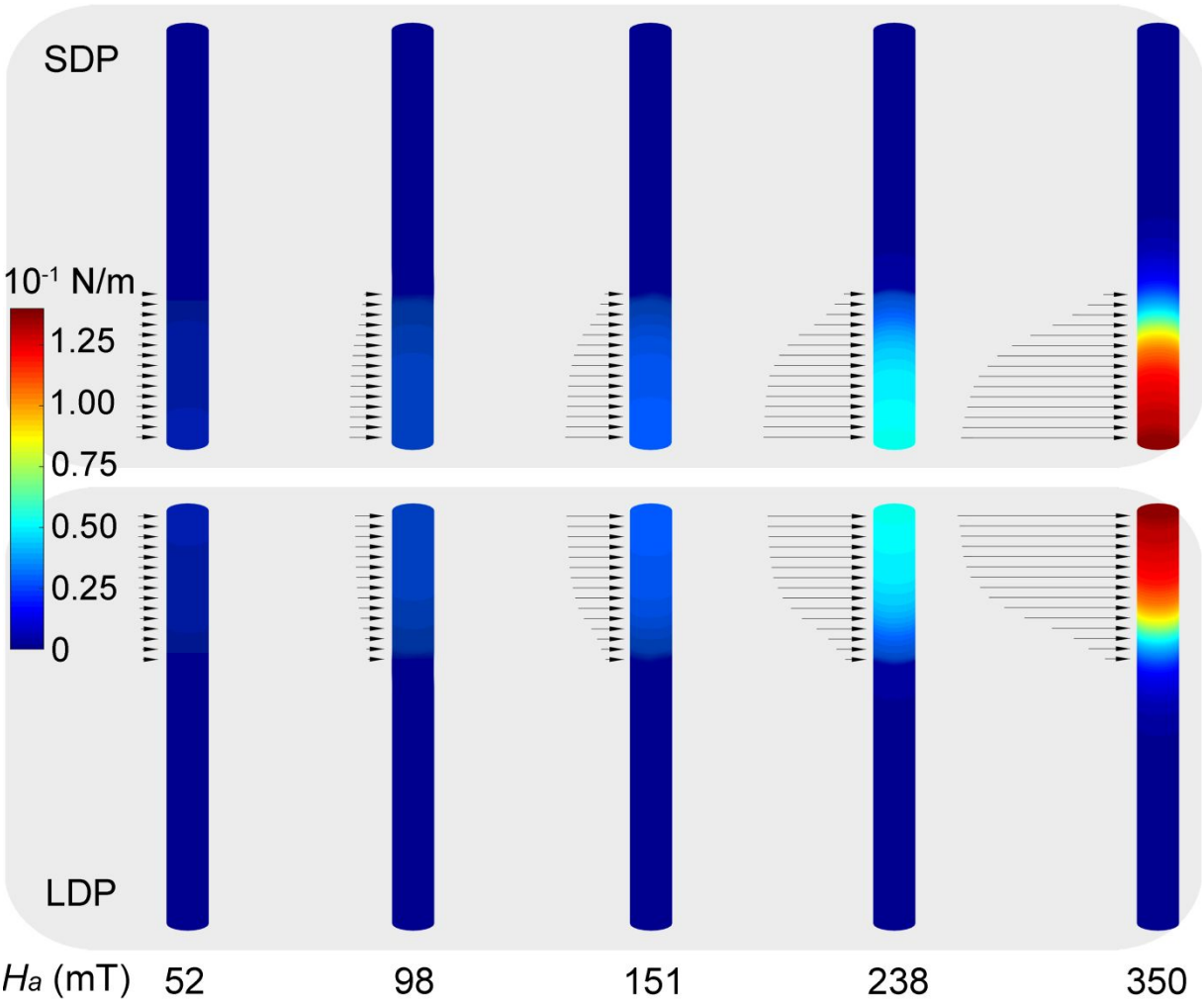

Figure S5. Theoretically calculated distributions of the actuation force along the resin channel of the SDP (top panel) and LDP (bottom panel) at different actuation fields ranging from ~50 mT, 5 mT/mm to 350 mT, 25 mT/mm (corresponding to the magnet-sample distance from 25 mm to 5 mm as shown in Figure S2) adopted in the experiments.

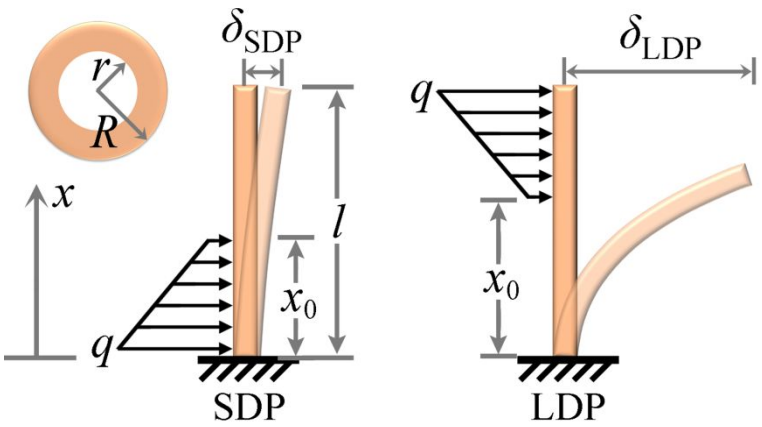

Figure S6. Schematic diagrams of the simplified models for the actuated bending of an SDP (left) and an LDP (right). Inset showing the cross-section of the circular hollow beam.

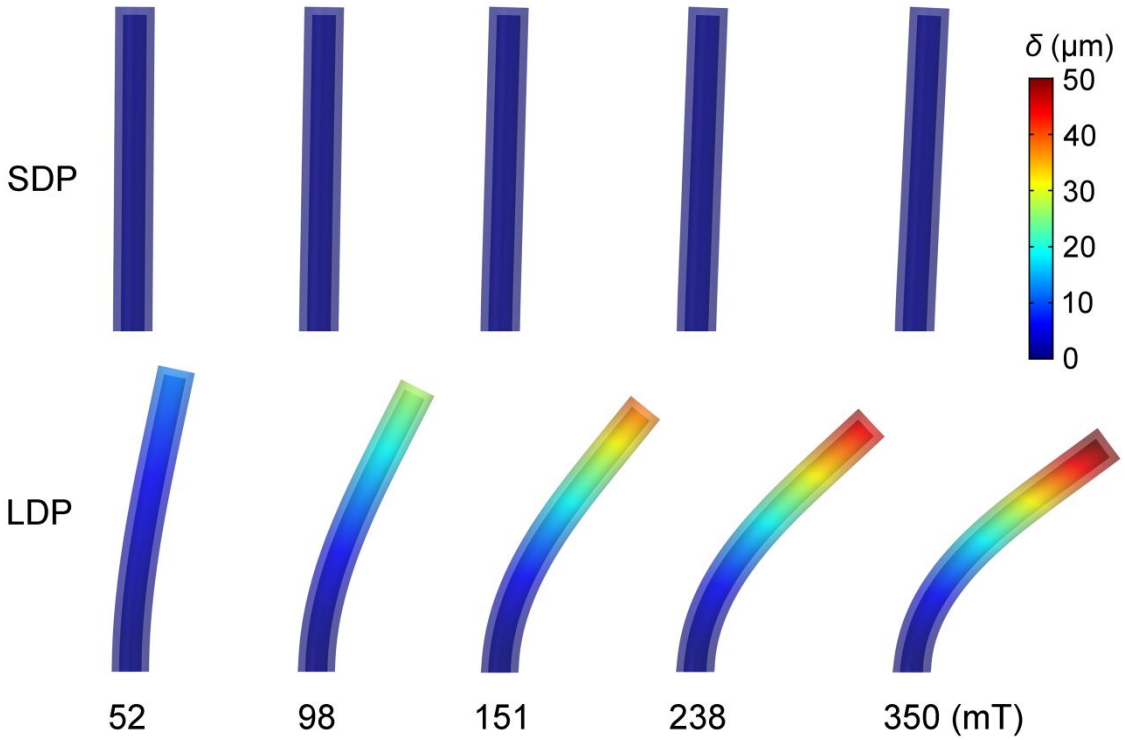

Figure S7. Numerical results of the bending deflections (δ) of the SDP (top panels) and LDP (bottom panels) at different actuation fields ranging from 50 mT, 5 mT/mm to 350 mT, 25 mT/mm (corresponding to the magnet-sample distance from 25 mm to 5 mm as adopted in the experiments) obtained by finite element analyses.

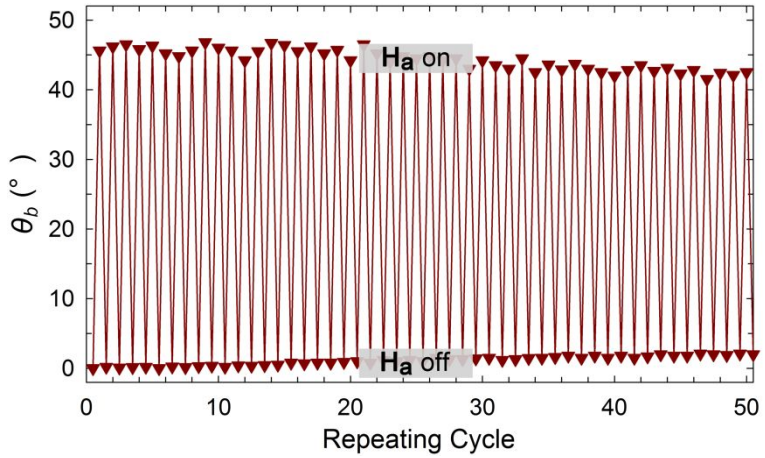

Figure S8. Results of repeated actuation tests showing the bending angle of the LDP as a function of the repeating cycle up to 50. The actuation field ($\mathbf{H_a}$) was periodically switched on by approaching the magnet towards the micropillars at an inter-distance of 5 mm and off by moving the magnet far away from the micropillars.

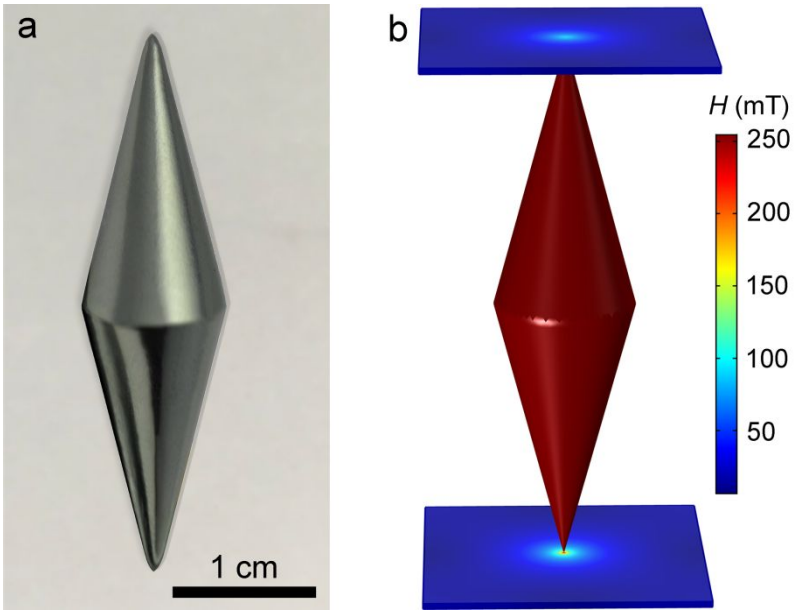

Figure S9. (a) Photograph of the symmetrical cone-shaped magnet (magnet needle) for the local nanoparticle modulations (magnetic writing). (b) Calculated magnetic field distribution at the tip regions of the magnetic needle that are used during the writings.

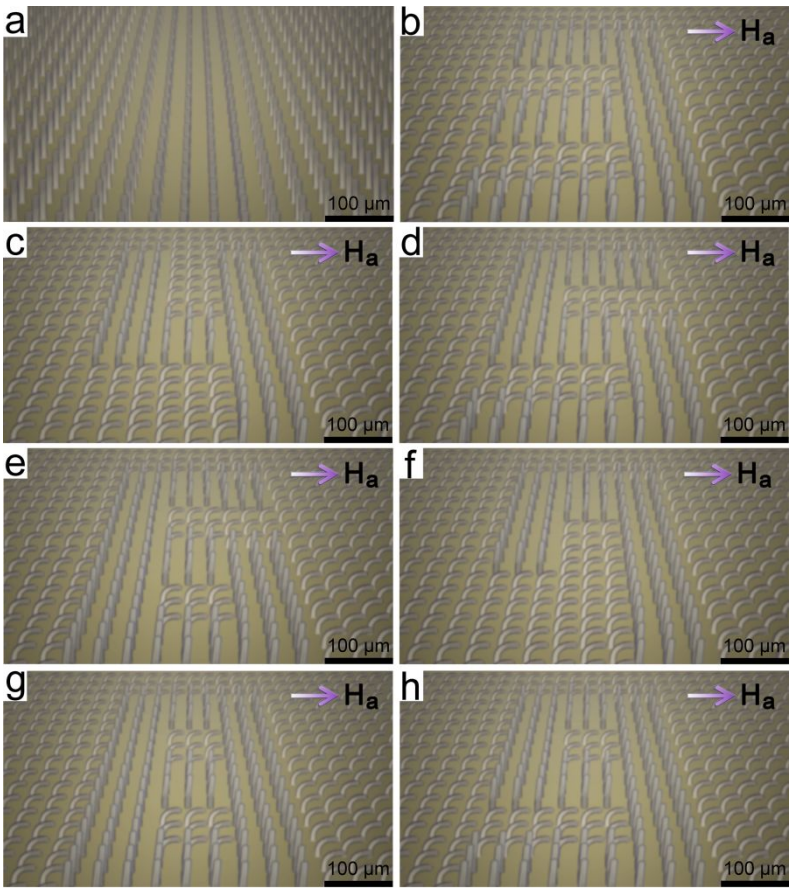

Figure S10. (a) Side-view optical microscope image of the erased core-shell magnetic micropillar array and (b-h) the corresponding images of the actuated array after repeatly erasing and writing with different Arabic numeral patterns from '3' to '9' at the same location. Short arrows indicate the direction of the actuation fields.

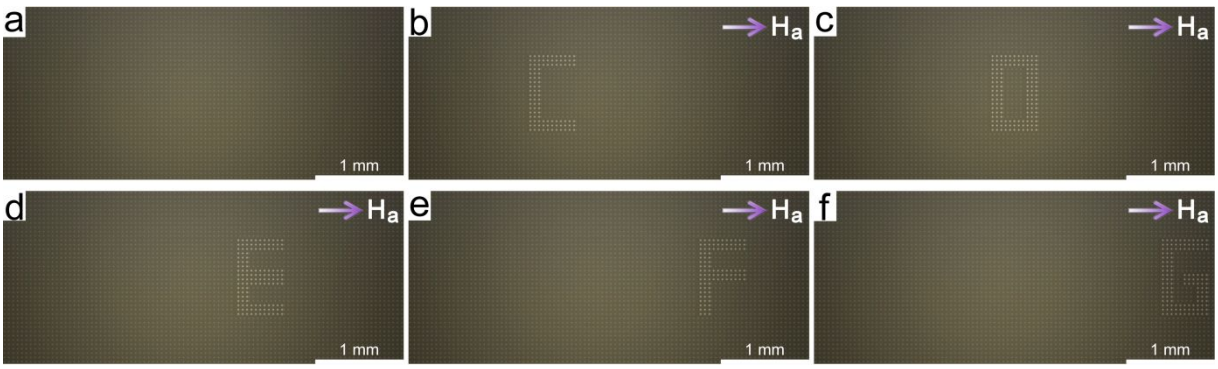

Figure S11. (a) Top-view optical microscope image of the erased core-shell magnetic micropillar array and (b-f) the corresponding images of the actuated array after repeatly erasing and writing with different English letters from 'C' to 'G' at sequential locations. Short arrows indicate the direction of the actuation fields.

Table S1. Parameters used in the calculations of the magnetic field, force, and concentration profiles of the magnetic nanoparticles during modulations.

$\eta = 0.16\ Ns/m^2$	$\rho_r = 1020\ kg/m^3$	$\rho_p = 5180\ kg/m^3$	$M_{sp} = 4.78\times10^5\ A/m$
$\mu_r = 1.26\times10^{-6}\ N/A^2$	$\mu_0 = 1.26\times10^{-6}\ N/A^2$	$\chi_r = 0$	$\chi_p = 0.6$
$k_B = 1.38\times10^{-23}\ J/K$	$R_p = 15\ nm$	$T = 300\ K$	$c_0 = 15\ vol.\%$
$M_{sm} = 1.04\times10^6\ A/m$	$h_m = 5\ mm$ $r_m = 30\ mm$	$l_m = 37\ mm$ $\theta_m = 30^o$ $\gamma_m = 100\ \mu m$	

η: viscosity of the PUA resin liquid;
ρ_r: density of the resin liquid;
ρ_p: density of the magnetic nanoparticle;
M_{sp}: saturation magnetization of the nanoparticle;
μ_r: permeability of the resin liquid;
μ_0: permeability of the free space;
χ_r: susceptibility of the resin liquid;
χ_p: susceptibility of the magnetic nanoparticle;
k_B: Boltzmann's constant
R_p: radius of a nanoparticle;
T: absolute temperature;
c_0: initial nanoparticle concentration in the UP;
M_{sm}: saturation magnetization of both the disk-shape magnet and the magnet needle;
h_m: thickness (height) of the disk-shape magnet;
r_m: radius of the disk-shape magnet;
l_m: length of the magnet needle;
θ_m: cone angle of the magnet needle;
γ_m: radius of curvature of the tips of the magnet needle.

Table S2. Parameters used in the calculations of the actuation forces, bending deflections, and bending angles for the SDP and LDP.

$l = 80\ \mu m$	$R = 5\ \mu m$	$r = 3\ \mu m$
$E = 8\ MPa$	$\nu = 0.5$	$G = 2.7\ MPa$
$q = 0.13\ N/m$	$x_0(SDP) = 30\ \mu m$	$x_0(LDP) = 50\ \mu m$

l: length of the micropillar;
R: outer radius of the micropillar;
r: inner radius of the micropillar;
E: elastic modulus of the pillar shell material;
v: Poisson's ratio of the pillar shell material;
G: shear modulus of the pillar shell material;
q: maximum distribution force applied to the pillar;
$x_0(SDP)$: x coordinate where the actuation force decreases to 0 along SDP;
$x_0(LDP)$: x coordinate where the actuation force starts to increase along LDP.

Movie Captions

Movie S1. Transformation dynamics of a micropillar transitioning from UP to SDP under an H_r of 200 mT, showing the gradual migration of the nanoparticles from the tip region to the base region inside the micropillar.

Movie S2. Transformation dynamics of a micropillar transitioning from UP to LDP under an H_r of 200 mT, showing the gradual migration of the nanoparticles from the base region to the tip region inside the micropillar.

Movie S3. Bending movie of a local SDP array upon magnet approaching and retracting.

Movie S4. Bending movie of a local LDP array upon magnet approaching and retracting.

Movie S5. Transformation dynamics of a micropillar transitioning from SDP to LDP under an H_r of 200 mT, showing the gradual migration of the nanoparticles from the base region to the tip region inside the micropillar.

Movie S6. Transformation dynamics of a micropillar transitioning from LDP to SDP under an H_r of 200 mT, showing the gradual migration of the nanoparticles from the tip region to the base region inside the micropillar.

Movie S7. Demonstration of a local actuation on a hybrid micropillar array consisting of half SDP and half LDP pattern.

Movie S8. Demonstration of a local actuation on a hybrid micropillar array consisting of alternating SDP and LDP (one SDP by one LDP) pattern.

Movie S9. Demonstration of the core-shell magnetic micropillar array applied as a rewritable paper. Various Arabic numeral patterns from '0' to '9' are repeatedly written on the array and then controlled to appear and disappear at the same location of the array by magnetic actuations and deactuations.

Movie S10. Demonstration of the core-shell magnetic micropillar array applied for recyclable displays. Various English letter patterns from 'A' to 'G' are repeatedly written and erased on the array and then controlled to dynamically display and conceal at sequential locations of the array by magnetic actuations and deactuations.

Movie S11. Demonstration of the recyclable display of a combination of the letters from 'A' to 'G' using the core-shell magnetic micropillar array.

Supplementary References

1. Chandrasekhar, S. Stochastic Problems in Physics and Astronomy. *Rev. Mod. Phys.* **1943**, *15*, 1-89.
2. Friedman, G.; Yellen, B. Magnetic Separation, Manipulation and Assembly of Solid Phase in Fluids. *Curr. Opin. Colloid. In.* **2005**, *10*, 158-166.
3. Timoshenko, S.P.; Goodier, J.N. *Theory of Elasticity*, 3rd ed.; McGraw-Hill: New York, 1970; pp. 41-60.
4. Cowper, G.R. The Shear Coefficient in Timoshenko's Beam Theory. *J Appl. Mech.* **1966**, *33*, 335-340.